Received: 28 March 2020 | Revised: 27 August 2020 | Accepted: 30 November 2020

DOI: 10.1002/we.2606



RESEARCH ARTICLE

WILEY

# Large eddy simulations of wind turbine wakes in typical complex topographies

Zhenqing Liu[1] | Shengyu Lu[1] | Takeshi Ishihara[2]

[1]School of Civil and Hydraulic Engineering, Huazhong University of Science and Technology, Wuhan, China

[2]Department of Civil Engineering, School of Engineering, University of Tokyo, Tokyo, Japan

**Correspondence**
Zhenqing Liu, School of Civil and Hydraulic Engineering, Huazhong University of Science and Technology, Wuhan, China.
Email: liuzhenqing@hust.edu.cn

**Funding information**
Project of Innovation-driven Plan in Huazhong University of Science and Technology, Grant/Award Number: 2017KFYXJJ141; National Natural Science Foundations of China, Grant/Award Number: 51978307

## Abstract

There is a need to clarify the coupling characteristics of terrain-induced wind fields and wind turbine-induced wake in wind farm micrositing. However, research investigating the effect of hill shape on this interaction is lacking. In addition, during the optimization of the layout of the turbines over topographies, the flow behind the turbines should be predicted in a fast way. After obtaining the wake flow of the turbine mounted on flat terrain and the flow over the topographies, there are mainly two superposition methods to predict the turbine wake flow over the topographies. One is to add the wind deficit following the location with a vertical distance of the hub height (D-line). The other is to add the wind deficit following the streamline starting from the turbine center (B-line). It remains unknown to what extent these two superposition methods can be adopted. Therefore, the effects of hill shape, wind turbine size, and turbine location are investigated. When the wind deficit, obtained from modeling the wake flow of the turbine mounted on flat terrain, is superposed following B-line, the results are overall better than those when following D-line.

KEYWORDS
complex terrain, interaction, LES, wind turbine wake

## 1 | INTRODUCTION

Wind energy is the most widely used and fastest growing new power generation technology, and it has been developed and applied on a global scale. Toward the end of 2018, the cumulative wind power was 591 GW globally, more than 23 times that at the end of 2001.[1] Currently, wind farms have been constructed in more than 90 countries including Asia, Europe, and the Americas. By the end of 2018, China, the United States, Germany, India, and Spain became the top five countries in terms of cumulative onshore wind power. In China, wind power accounts for 5.23% of the total power consumption of the country, thereby making it the third largest power source after coal and hydropower.[1] However, owing to its continuous expansion, wind power is facing new challenges in China. The most prominent problem is the mismatch between the location of wind resources and power consumption. The northeast, northwest, and north of China are rich in wind resources and have flat terrains. Although many large wind farms have been installed in these areas, their power consumption is relatively low. The central, eastern, and southern regions of China have a high electricity consumption, but the terrain is complex. Therefore, as a response, the National Energy Administration of China issued the

**Abbreviations:** 2D, two-dimensional; 3D, three-dimensional; ADM-R, actuator disc model with rotation; BEM, blade element theory; CFD, computational fluid dynamics; CFL, Courant–Friedrichs–Lewy; FVM, finite volume method; GA, genetic algorithm; LES, large eddy simulation; N-S, Navier–Stokes; r.m.s., root mean square; RANS, Reynolds-averaged Navier–Stokes; SGS, subgrid scale; SIMPLE, semi-implicit pressure linked equations; TBL, turbulent boundary layer.

"13th Five-Year Plan for Wind Power Development"[2] based on the principle of "near resources, local consumption," which clearly states it is necessary to accelerate the development of onshore wind energy in complex terrain in the central, eastern, and southern regions of China.[2]

The experimental studies of the effects of terrain on wind turbine wake began in the early 1990s. To our knowledge, Taylor and Smith[3] conducted the first wind-tunnel experiment to reveal the effects of topography on flow fields in the wind turbine wake. In that experiment, the terrain was a flat-topped two-dimensional (2D) hill, and the model wind turbine was installed in several positions. Englberger and Dörnbrack[4] investigated the wind turbine wake in complex terrain under various atmospheric conditions, and they found that the advective transport of turbulence was crucial. Hyvärinen and Segalini[5] carried wind-tunnel experiments. In that study, velocity profiles behind the turbine showed that the wake recovery was more rapid in the cases with hills, compared with the plain configuration cases. Astolfi et al.[6] also found faster wake recovery for the turbine over complex terrain with respect to flat terrain. From experiments and simulations by Castellani et al.,[7] the main effect of the terrain was mainly for the upstream turbine, and the presence of the rest of the subcluster deviated the wake line of the upstream turbine. Hyvärinen et al.[8] investigated wake development on sinusoidal hills using particle image velocimetry (PIV). The introduction of terrain enhanced the downward deflection of the wake and the wind fluctuation. Further, they pointed out that when the analytical wake model was used over hilly terrain, an accurate turbulence model was found to be essential for capturing wake development. Tian et al.[9] studied the wake of five turbines placed in an array on a 2D hill with slopes (defined as hill height over half of hill length) of 0.25 and 0.5. Compared to results for wind turbines on flat ground, the wind turbines installed on the hillcrest not only extracted more wind energy because of the acceleration effects but also reduced the fatigue load. Rapid recovery of the wind turbine wake was also observed. Howard et al.[10] examined the terrain effects on the wind turbine wake, and the upwind hill was found to cause a reduction in the mean angular velocity. Kozmar et al.[11,12] studied the effects of complex terrain shape on the wakes of wind turbines installed downstream of these topographies. Further, a ridgelike topography, with or without a bay at the center, was examined.

The wake evolution of multi-megawatt wind turbines, located in both flat and complex terrains, was revealed using drone-based measurements by Subramanian et al.[13] It was observed that in complex terrain, the near-wake extent of the wind deficit was shorter. Furthermore, Han et al.[14] investigated the effects of topography and atmospheric stability and found that when the terrain shape was complex or the air was in an unstable state, turbulence was enhanced and the wind deficit in the wind turbine wake recovered faster. Using light detection and ranging (LiDAR) measurements and supervisory control and data acquisition (SCADA), Gao et al.[15] conducted several field measurements of wind turbine wake in complex terrain; the results showed that the steeper and longer the slope, the more visible is the wind speed-up effect and the greater is the wake recovery compared to a flat terrain. Sun et al.[16] measured wind turbine wake in complex terrain and compared the results to an analytical model.[17] They found that the analytical model performed poorly in near-wake regions. They concluded that complex terrain made the inflow distribution too complicated to be well described by the analytical model, which results in worse predictions.

During the last 10 years, there has been a rapid increase in the number of numerical studies on wake–terrain interactions owing to the advancement of computer technology. Politis et al.[18] used $k$–$\varepsilon$ and $k$–$\omega$ closures to study the effects of topography on wake evolution and modeled wind turbines with the actuator disc method. They found that linear superposition approaches are not sufficiently robust to predict the wind speed deficit or wake shape. Further, it was observed that faster recovery of wake losses would result from an increase in turbulence intensity because of topography. Makridis and Chick[19] used the commercial software Fluent and assumed a three-dimensional (3D) stationary flow using the Reynolds-averaged Navier–Stokes (RANS) equations. Their results produced errors within 20% in the far-wake region as compared with field observation data for the averaged velocities. Using the RANS model, Nedjari et al.[20] further examined the interactions between topography and wake. Their simulation results are in good agreement with the wind-tunnel experimental results. Shamsoddin and Porté-Agel[21] developed code using the finite difference method (FDM) and large eddy simulations (LES) to model turbines on typical terrains. LES was found to be effective in reproducing the flow fields, which were characterized by increased speed around the hilltop, a wake velocity deficit, and enhanced turbulence intensity. Three different turbulence models—the standard, RNG, and realizable $k$–$\varepsilon$ models—were set up and discussed by Murali and Rajagopalan.[22] The realizable $k$–$\varepsilon$ model performed best in the comparisons. The power output of a wind farm in complex terrain was modeled by adopting LES,[23] and the simulations exhibited good agreement with experimental data. They also compared the analytical wake model without accounting for complex terrain effects, which resulted in overestimation of the wind power output. Yan et al.[24] utilized the standard $k$–$\varepsilon$ model to investigate the wake flow around hills with different slopes and observed stronger diffusion of the wake. They concluded that the coupling between wind turbines and terrain must be taken into account when determining the site of wind farms. Meanwhile, a modified delayed detached eddy simulation (MDDES) was developed and adopted to model wind turbine wakes over escarpments by Qian and Ishihara[25]; their results show satisfactory agreement with the LiDAR measurements. Shamsoddin and Porte-Agel[26] presented an analytical modeling framework together with LES results to investigate turbine wakes over 2D hills. This model enables us to obtain the wake recovery rate, the mean velocity and velocity deficit profiles, and the wake trajectory in the presence of the hill.

Our research group examined the modeling of flow fields over typical topographies extensively[27–32]; however, we did not study the interactions between wind turbine wake and flow fields over various topographies. The literature survey indicated that even though the number of studies on the interaction between wind turbines and terrain has increased in recent years, there is yet no study considering the different features of the interaction between wind turbines and topographies with different shapes such as 3D and 2D hills.

In addition, for any optimization of turbine layout in an onshore wind farm, it has to firstly obtain the flow fields over the terrain. After obtaining the flow fields over the terrain, we can superpose analytical wake model (without considering the terrain effects) on the obtained flow fields over terrain. But we have to understand where to do the superposition. That is what will be examined in the present study. Of course during the iteration of the optimization, the flow field can be simulated considering both the terrain and turbine effects. But the steps of the iteration are always over 2000, and if we do the simulation at each step, the computational time cannot be afforded. Therefore, in the real application, what can be done is to model the turbine wake flow and terrain flow separately and then use superposition method to estimate the turbine wake flow over terrain and do the optimization of turbine layout in an onshore wind farm. Up to now, there are mainly two superposition methods to reproduce the turbine wake flow over the topographies. One is to add the wind deficit caused by the turbine following the location with a vertical distance of the hub height. The other is to follow the streamline starting from the turbine center. However, it remains unknown to what extent the superposition methods can be adopted. In the present study, this question will be clarified.

The rest of this manuscript are organized as follows. The numerical model is presented first in Section 2. Flow fields over hills without the involvement of wind turbines, the interaction between wind turbines and hills, and the condition for the application of the superposition method are introduced in Section 3. Section 4 summarizes the findings in the present study and gives the research direction in the future.

## 2 | NUMERICAL MODEL

In Section 2.1, the modeling approach of the wind turbines is presented. Section 2.2 describes the settings of the computational domain and grid system, followed by the introduction of the boundary condition, solution method, and case settings.

### 2.1 | Methodology

LES is used, and standard Smagorinsky–Lilly model[23,24] is adopted. The Smagorinsky constant $C_s$ is determined to be 0.1 following Liu and Ishihara.[28] The actuator disc model with rotation (ADM-R) is adopted to consider the effects of rotor-induced force on flow fields; lift and drag forces are determined based on the blade element theory (BEM) (Burton et al.[33]), and then, it is unevenly distributed on the actuator disc. The wind turbine examined here is the Mitsubishi MWT-1000, because of the availability of detailed aerodynamic information, including the lift ($C_L$) and drag ($C_D$) force coefficients in terms of angle of attack, as introduced by Ishihara and Qian.[34] The rotor diameter of the MWT-1000, $D_f$, is 57 m; the hub height, $h_f$, is 70 m; the tip speed ratio in operation, $\lambda$, is 9.69; and the resulting thrust force coefficient, $C_T$, is 0.81. $\lambda$ and $C_T$ are the values at the wind speed that is investigated. The key structural parameters of this wind turbine are listed in Table 1.

### 2.2 | Computational domain and grid

A schematic view of the simulated domain is shown in Figure 1, wherein $x$ lies along the streamwise, $y$ along the spanwise, and $z$ along the vertical coordinate axis. Besides the spanwise direction and nozzle region near the inlet, the geometrical settings of the numerical model are the same as those of the wind-tunnel experiments of Ishihara et al.,[35,36] where the turbulent boundary layer (TBL) is modeled by roughness blocks. The roughness blocks comprise two each of 10, 20, and 60 mm$^3$ arrays, covering 1.2 m$^2$ of the ground. At a distance of 3.4 m downstream from the roughness blocks, the 3D and 2D hills with radius $L$ = 0.1 m were mounted; the center of the topographies on the floor was set as the origin (0, 0, 0) of the model. In the present LES, the domain covers 9, 0.65, and 0.9 m$^3$. The geometrical parameters of the simulated domain are summarized in Table 2.

A mesh system with hybrid-grid densities is designed to minimize the calculation time while maintaining prediction accuracy. This system is shown in Figure 2A. The fine-grid domain covers the region within $-0.5\ \text{m} < x < 0.5\ \text{m}$, $-0.1\ \text{m} < y < 0.1\ \text{m}$, and $0.0\ \text{m} < z < 0.9\ \text{m}$. In the fine-grid domain, a grid size of 2.0 mm in the horizontal direction was adopted after a grid independency examination. The horizontal grid size was reduced with cells number doubling to 2 mm from 10 mm for the grid independency (Section 3.1). The total number of cells is about $2.5 \times 10^7$. A buffer region near the boundary wall between the fine-grid domain and the coarse-grid domain is used to avoid sudden changes in grid size. The horizontal grid size at the inner boundary of the buffer region is equal to that in the fine-grid region, and the size at the outer boundary of the buffer region is equal to that in the coarse-grid region. A growth factor of 1.2 is used to change the grid size in the buffer zone. Vertical grid sizes for the

**TABLE 1** Key parameters of the wind turbine

| Wind turbine type | Tip speed ratio $\lambda$ | Thrust force coefficient $C_T$ | Rotor diameter $D_f$ (m) | Hub height $h_f$ (m) |
|---|---|---|---|---|
| Mitsubishi MWT-1000 | 9.69 | 0.81 | 57 | 70 |

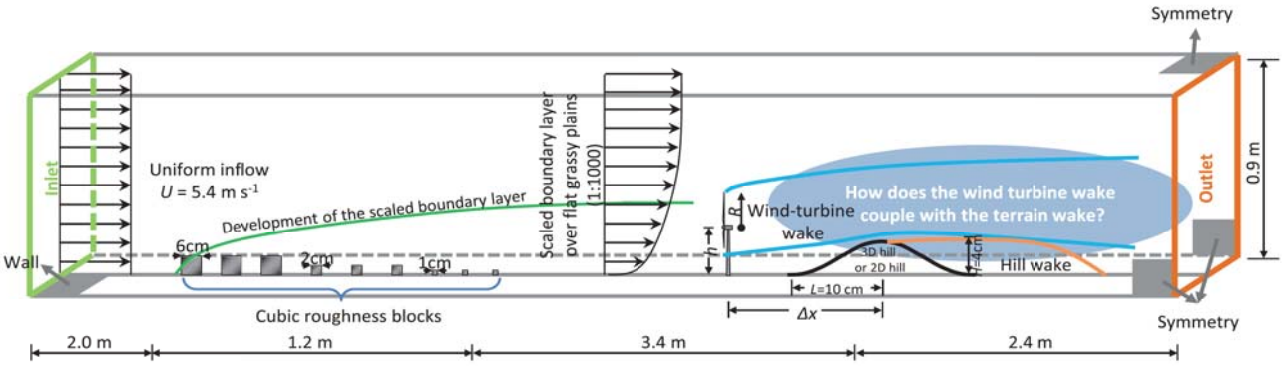


**FIGURE 1** Schematic of the computational domain and boundary conditions

**TABLE 2** Geometrical parameters of the computational domain

| Length of the domain ($L_x$) (m) | Width of the domain ($L_y$) (m) | Height of the domain ($L_z$) (m) | Length of the fine-grid domain ($L_{fx}$) (m) | Width of the fine-grid domain ($L_{fy}$) (m) | Height of the fine-grid domain ($L_{fz}$) (m) |
|---|---|---|---|---|---|
| 9.0 | 0.65 | 0.9 | 1.0 | 0.2 | 0.9 |

fine-grid and coarse-grid domains are the same; this is stretched by a factor of 1.05 from 0.1 mm at the surface. A $\sigma$-grid system is utilized to vary the positions of vertical cell nodes while maintaining the size ratio of the vertical grids to the adjacent grids unchanged.

When the actuator wake model and the LES turbulence modeling method are adopted, it is necessary to ensure that ~20 grid points span the rotor diameter to reproduce the wind turbine-induced wake flow accurately.[37] In the present LES, three rotor sizes are examined, and the wind turbine is mounted at locations $x$ = −0.2, −0.1, and 0.0. The grid distribution for rotors with different mounting locations are shown in Figure 2; for the smallest and largest rotors, there are about 20 and 50 cells covering the rotor diameter. The grid information for the computational domain is summarized in Table 3.

## 2.3 | Boundary conditions

The stress-free boundary condition is adopted at the lateral and top surfaces of the computational domain, that is, $\partial\tilde{u}/\partial n = 0$, $\partial\tilde{v}/\partial n = 0$, $\tilde{w} = 0$ for the top and $\partial\tilde{u}/\partial n = 0$, $\partial\tilde{w}/\partial n = 0$, $\tilde{v} = 0$ for the lateral sides, respectively. A uniform wind speed of 5.4 m s$^{-1}$ is set at the inlet ($\tilde{u}$ = 5.4 m s$^{-1}$, $\partial\tilde{p}/\partial n = 0$) as the inflow condition. At the outlet, the gradient-free condition is used ($\partial\tilde{u}_i/\partial n = 0$, $\partial\tilde{p}/\partial n = 0$). At the ground, a nonslip condition is applied ($\tilde{u}_i = 0$, $\partial\tilde{p}/\partial n = 0$), and the $y^+$ value of the cell at the ground is less than 2.0.

## 2.4 | Solution scheme and solution procedure

The N–S governing equations with an unsteady 3D LES filter were calculated by Ansys Fluent 14.0[38] using the finite volume method (FVM). Convective and viscous terms in the momentum equations were discretized by the second-order central difference scheme; the unsteady terms were discretized using the second-order implicit scheme. The time step size in Ansys Fluent, $\Delta t$, was 0.0001 s, which resulted in convective time units, $\Delta t^* = \Delta t\, U_0/L = 0.0058$. The Courant–Friedrichs–Lewy (CFL) number, expressed as $C = \Delta t \Sigma \tilde{u}_i/\Delta\chi_i$, where $\Delta\chi_i$ is the cell size,[39] was limited to less than 1 in the entire domain of the simulations. The semi-implicit pressure linked equation (SIMPLE) algorithm was adopted to uncouple the solution of pressure and velocities. The calculations were run by six paralleled PCs with Intel core i9-7980XE 18-core CPUs and 64-Gb memory. In all simulations, the initial transient effects disappeared after 400 time units. After stability was achieved, the averaged turbulent fields were then obtained during the following 600 time units. The numerical schemes and computational resources in the present LES are listed in Table 4.

## 2.5 | Case settings

In this study, the wind turbine is mounted at locations upstream from the hills and hill summits, with longitudinal distances between the hill summit and the rotor center being 2, 1, and 0 $L$. This is because in the initial phase of location selection in complex terrain, locations downstream from hills are rarely selected.

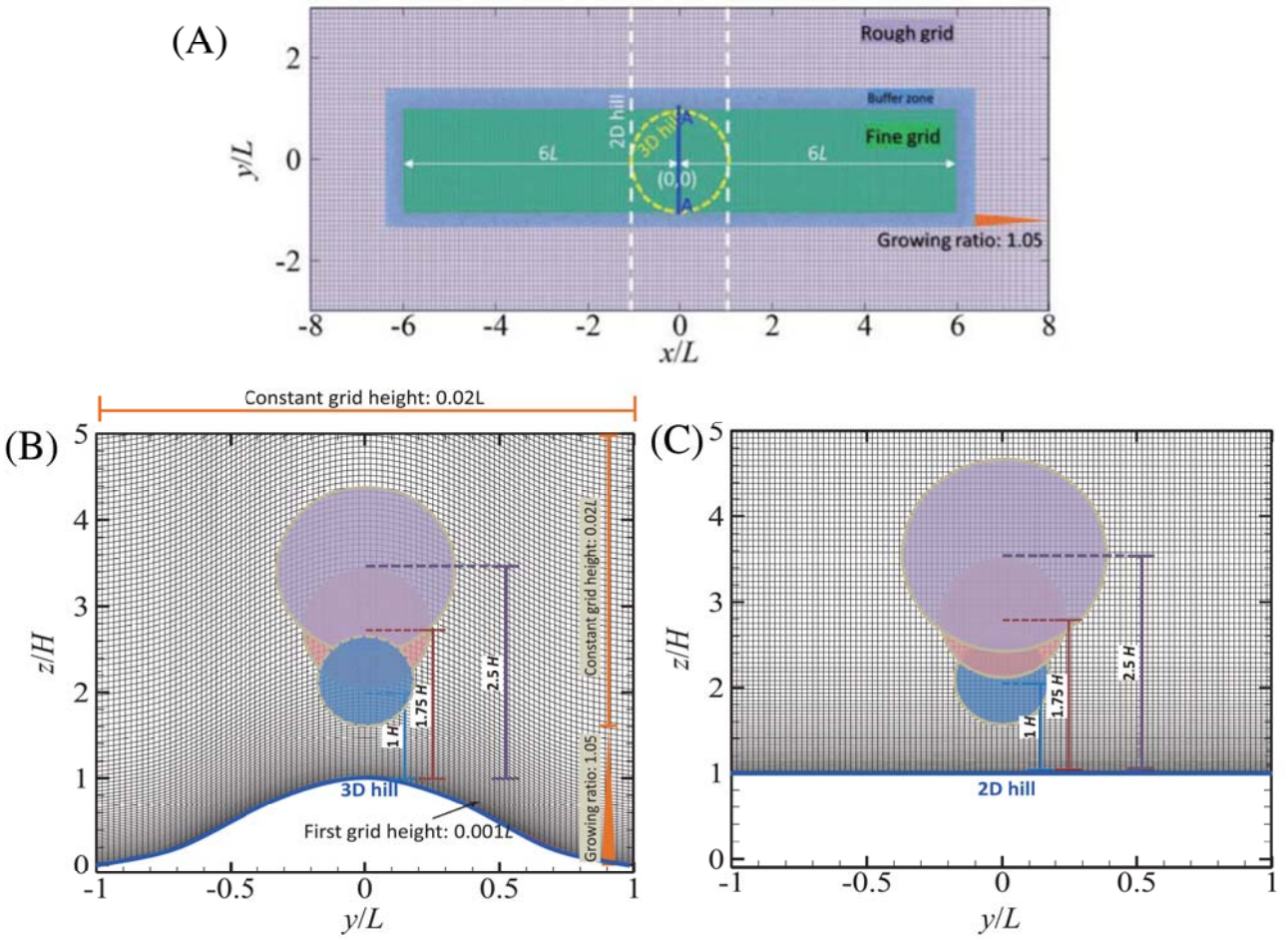


**FIGURE 2** Grid distribution (A) horizontal plane, (B) cross section A-A with a 3D hill mounted at (0, 0), and (C) cross section A-A with a 2D hill mounted at (0, 0)

**TABLE 3** Grid parameters of the numerical model

| Grid type | Minimum horizontal cell size (mm) | Maximum horizontal cell size (mm) | Minimum vertical cell size (mm) | Maximum vertical cell size (mm) | Maximum horizontal increasing ratio | Maximum vertical increasing ratio | Number of cells covering the rotor diameter | Grid number |
|---|---|---|---|---|---|---|---|---|
| Hexahedron grid | 2.0 | 10 | 0.1 | 20 | 1.2 | 1.05 | 20–50 | $\approx 2.5 \times 10^7$ |

Two typical complex topographies—3D hill and 2D hill, which have been extensively investigated in previous wind-tunnel experiments[40–44] and in several numerical simulations[45–52]—were selected to clarify the effects of the topography shape on the interactions between the wind turbine and the terrains. The 3D and 2D hills are located at (0, 0, 0). The shape of the 3D hill is determined according to

$$\begin{cases} z_s(x,y) = H\cos^2\pi\left(x^2+y^2\right)^{1/2}/2L, & \text{if } \left(x^2+y^2\right)^{1/2} < L \\ z_s(x,y) = 0, & \text{if } \left(x^2+y^2\right)^{1/2} \geq L \end{cases} \tag{1}$$

where $L$ represents a constant of 100 mm and $H$ = 40 mm. The shape of the 2D hill is specified using

$$\begin{cases} z_s(x,y) = H\cos^2\pi|x|/2L, & \text{if } |x| < L \\ z_s(x,y) = 0, & \text{if } |x| \geq L \end{cases} \tag{2}$$

**TABLE 4** Numerical schemes

| | | | |
|---|---|---|---|
| Time discretization scheme | Second-order implicit scheme | SGS model | Smagorinsky–Lilly |
| Space discretization scheme | FVM second-order central difference scheme | CFL number | <2 |
| $\Delta t\ U_0/L$ | ≈0.0058 | Decoupling method | SIMPLE |
| Simulation method | LES | Software | Ansys Fluent 14.0 |
| Time for statistics | 10 s | CPU | 6PCs in parallel Intel core i9-7980XE, 18 cores |
| Smagorinsky constant $C_s$ | 0.1 | Memory | 64 Gb |

A second vertical coordinate, $z' = z - z_s\,(x, y)$, represents the height above the local surface; a second streamwise coordinate $x'$ denotes the downstream distance from the wind turbine.

The wind turbine is scaled to have hub heights ($h$) equal to $1H$ (turbine T1), $1.75H$ (turbine T2), and $2.5H$ (turbine T3) to study the effect of the size of the wind turbine relative to that of the hill. A schematic view of the cases is shown in Figures 3 and 4.

To facilitate the understanding of the interaction effects between the wind turbine and the topographies, additional cases were simulated for the hills without any wind turbines. Further, simulations with wind turbines mounted on flat terrain were conducted to provide a basic wind speed deficit for use in the examination of the superposition method.

Cases 2L3DT1 and 0L2DT3 were selected for grid independency examinations because these cases include 3D and 2D hills, the smallest and largest wind turbines, and the maximum and minimum distances to the hill. Six increasingly refined cells were adopted in each case. The case settings, case names, and key parameters are listed in Table 5.

## 3 | NUMERICAL RESULTS

### 3.1 | Grid independence

Six increasingly refined grids—numbered Grid 1 ($G_1$) to Grid 6 ($G_6$) with parameters as summarized in Table 6—were generated to perform detailed grid convergence tests and specify mesh independence. To describe grid independence clearly and quantitatively, the relative errors of the mean streamwise velocities, $\epsilon_U$, and turbulence intensities, $\epsilon_I$, were calculated. The relative errors were expressed as

$$\epsilon_U = \frac{\int_{x'=0}^{x'=4L}\int_{z'=0}^{z'=5H} |U_{G_{n+1}} - U_{G_n}|\,dz'dx'}{\int_{x'=0}^{x'=4L}\int_{z'=0}^{z'=5H} |U_{G_n}|\,dz'dx'} \tag{3}$$

$$\epsilon_I = \frac{\int_{x'=0}^{x'=4L}\int_{z'=0}^{z'=5H} |I_{G_{n+1}} - I_{G_n}|\,dz'dx'}{\int_{x'=0}^{x'=4L}\int_{z'=0}^{z'=5H} I_{G_n}\,dz'dx'} \tag{4}$$

where $U_{G_{n+1}}$ and $U_{G_n}$ indicate the mean streamwise velocity at grid levels $n + 1$ and $n$, respectively, and $I_{G_{n+1}}$ and $I_{G_n}$ indicate the turbulence intensity at grid levels $n + 1$ and $n$, respectively. $\epsilon_U$ and $\epsilon_I$ as a function of the grid number are shown in Figure 5, where it is clear that the relative errors are less than 5% at grid Levels 5 and 6 for different scenarios, and therefore, the finest grid system $G_6$ is adopted in all cases in the present LES.

### 3.2 | Neutral atmospheric boundary layer

In the absence of topographies and wind turbines, the time-averaged streamwise velocity, $U$, and root mean square (r.m.s.) of the streamwise, spanwise, and vertical velocity fluctuations, $u$, $v$, and $w$, respectively, are compared to the experiments of Ishihara et al.,[36] as plotted in Figure 6. The profiles are normalized by $U_{ref}$, which is the time-averaged streamwise velocity at $z' = 4H$; it is equal to 5.3 m $s^{-1}$ in the LES results and 5.2 m $s^{-1}$ in the experimental results. For all statistics, apparent discrepancies occur below $z'$ = 10 mm, which is extremely close to the ground. The reason for these discrepancies may be the disturbance of fluids resulting from probes in the experiment. The discrepancies are mostly below 5%. The created neutrally stratified atmospheric boundary layer (ABL) simulation is uniform in the streamwise direction in the range $-6\ L < x < 6\ L$. The length scale 1:1000 is determined using Cook's[53] approach, countering the roughness length $z_0$ and integral length scale $L_{u,x}$. In

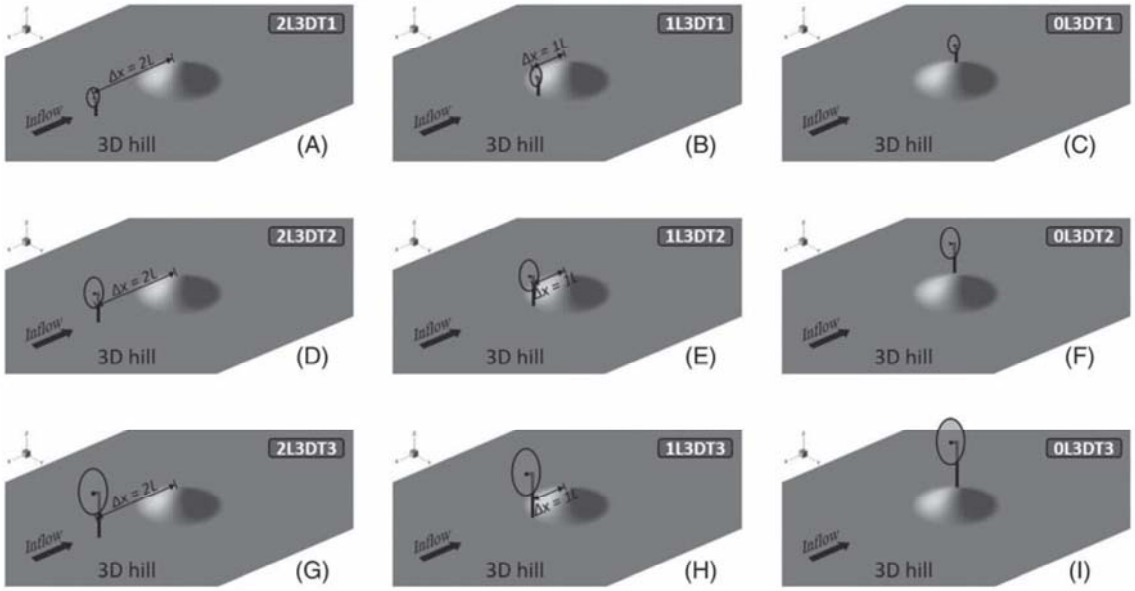


**FIGURE 3** Illustrations of the cases for the examinations of the interactions between 3D hill and wind turbines. (A) 2L3DT1, (B) 1L3DT1, (C) 0L3DT1, (D) 2L3DT2, (E) 1L3DT2, (F) 0L3DT2, (G) 2L3DT3, (H) 1L3DT3, and (I) 0L3DT3

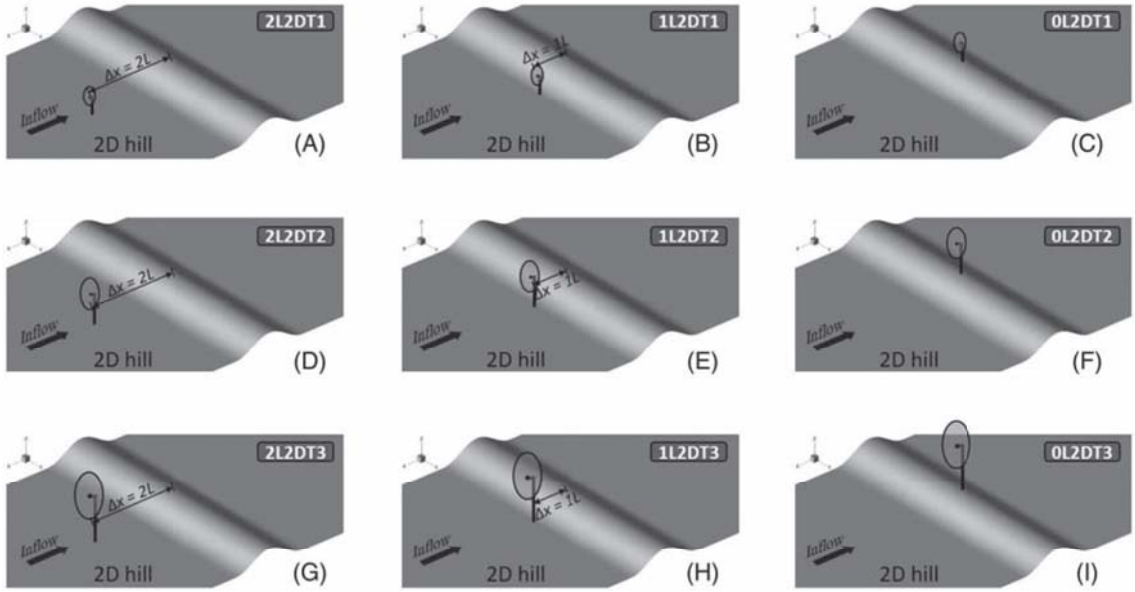


**FIGURE 4** Illustrations of the cases for the examinations of the interactions between 2D hill and wind turbines. (A) 2L2DT1, (B) 1L2DT1, (C) 0L2DT1, (D) 2L2DT2, (E) 1L2DT2, (F) 0L2DT2, (G) 2L2DT3, (H) 1L2DT3, and (I) 0L2DT3

simulations without a complex terrain or wind turbine, $z_0$ = 0.01 mm and the power-law exponent of the mean streamwise velocity $\alpha_0$ = 0.185 were determined by the fitting procedure, similar to that in the wind-tunnel studies of Ishihara et al.[36] In the full-scale model, the roughness length $z_0$ = 10 mm and the power-law exponent $\alpha_0$ = 0.185 correspond to onshore flat grassy plains.[33]

### 3.3 | Flow fields over typical topographies

For comparison with flow fields after the inclusion of the wind turbines, flow fields over topographies without wind turbines are briefly presented in this section.

**TABLE 5** Case settings

| Case name | Longitudinal distance between wind turbine and hill ($\Delta x/L$) | Scale of the wind turbine ($\lambda_w$) | Diameter of the rotor ($D$) (cm) | Hub height ($h$) (cm) | Terrain shape | Grid independency examination |
|---|---|---|---|---|---|---|
| 2L3DT1 | 2 | 1:1750 | 3.25 | 4 | 3D hill | • |
| 2L3DT2 | 2 | 1:1000 | 5.70 | 7 | 3D hill | ◦ |
| 2L3DT3 | 2 | 1:700 | 8.14 | 10 | 3D hill | ◦ |
| 2L2DT1 | 2 | 1:1750 | 3.25 | 4 | 2D hill | ◦ |
| 2L2DT2 | 2 | 1:1000 | 5.70 | 7 | 2D hill | ◦ |
| 2L2DT3 | 2 | 1:700 | 8.14 | 10 | 2D hill | ◦ |
| 1L3DT1 | 1 | 1:1750 | 3.25 | 4 | 3D hill | ◦ |
| 1L3DT2 | 1 | 1:1000 | 5.70 | 7 | 3D hill | ◦ |
| 1L3DT3 | 1 | 1:700 | 8.14 | 10 | 3D hill | ◦ |
| 1L2DT1 | 1 | 1:1750 | 3.25 | 4 | 2D hill | ◦ |
| 1L2DT2 | 1 | 1:1000 | 5.70 | 7 | 2D hill | ◦ |
| 1L2DT3 | 1 | 1:700 | 8.14 | 10 | 2D hill | ◦ |
| 0L3DT1 | 0 | 1:1750 | 3.25 | 4 | 3D hill | ◦ |
| 0L3DT2 | 0 | 1:1000 | 5.70 | 7 | 3D hill | ◦ |
| 0L3DT3 | 0 | 1:700 | 8.14 | 10 | 3D hill | ◦ |
| 0L2DT1 | 0 | 1:1750 | 3.25 | 4 | 2D hill | ◦ |
| 0L2DT2 | 0 | 1:1000 | 5.70 | 7 | 2D hill | ◦ |
| 0L2DT3 | 0 | 1:700 | 8.14 | 10 | 2D hill | • |
| 3D hill | | \ | \ | \ | 3D hill | ◦ |
| 2D hill | | \ | \ | \ | 3D hill | ◦ |
| T1-flat | \ | 1:1750 | 3.25 | 4 | Flat | ◦ |
| T2-flat | \ | 1:1000 | 5.70 | 7 | Flat | ◦ |
| T3-flat | \ | 1:700 | 8.14 | 10 | Flat | ◦ |

*Note*: • means yes, ◦ means no, and means the cases for grid independency examination.

**TABLE 6** Parameters in grid independency examinations

| Case name | Grid level ($n$) | Horizontal grid size in fine-grid domain (mm) | Number of cells | Time for calculation (h) |
|---|---|---|---|---|
| 2L3DT1-1 | 1 | 10.0 | $\approx 7.5 \times 10^5$ | 25 |
| 2L3DT1-2 | 2 | 8.0 | $\approx 1.5 \times 10^6$ | 37 |
| 2L3DT1-3 | 3 | 5.6 | $\approx 0.3 \times 10^7$ | 65 |
| 2L3DT1-4 | 4 | 4.0 | $\approx 0.6 \times 10^7$ | 123 |
| 2L3DT1-5 | 5 | 2.8 | $\approx 1.2 \times 10^7$ | 260 |
| 2L3DT1-6 | 6 | 2.0 | $\approx 2.4 \times 10^7$ | 491 |
| 0L2DT3-1 | 1 | 10.0 | $\approx 7.5 \times 10^5$ | 25 |
| 0L2DT3-2 | 2 | 8.0 | $\approx 1.5 \times 10^6$ | 37 |
| 0L2DT3-3 | 3 | 5.6 | $\approx 0.3 \times 10^7$ | 65 |
| 0L2DT3-4 | 4 | 4.0 | $\approx 0.6 \times 10^7$ | 123 |
| 0L2DT3-5 | 5 | 2.8 | $\approx 1.2 \times 10^7$ | 260 |
| 0L2DT3-6 | 6 | 2.0 | $\approx 2.4 \times 10^7$ | 491 |

The contours of instantaneous vorticity in the $y$ direction, $\omega_y = \partial\tilde{w}/\partial x - \partial\tilde{u}/\partial z$, mean streamwise velocity $U$, r.m.s. of the streamwise fluctuations $u$, the streamlines, and the profiles of $U$ and $u$ on the $y = 0$ slice are presented in Figures 7 and 8. From $\omega_y$ (Figures 7A and 8A), it is apparent that there are many high-intensity vortices in the wake of the 3D and 2D hills; however, when the fluid is moving downstream, the turbulence generated by the 3D hill is much weaker than that by the 2D hill.

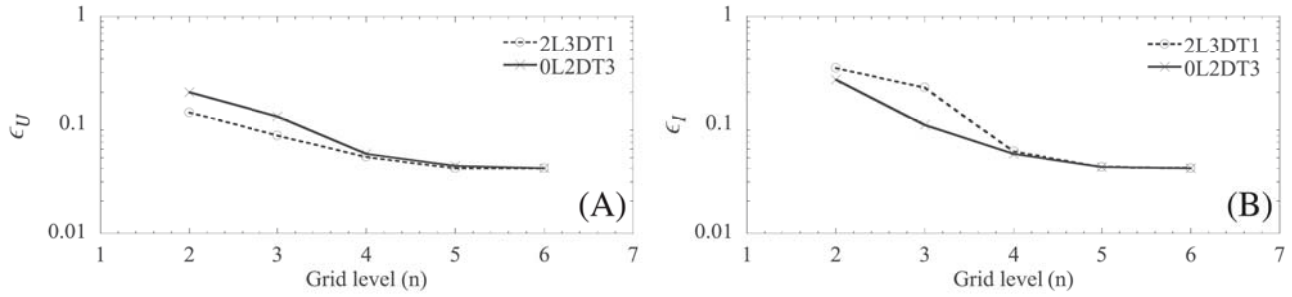


**FIGURE 5** Relative errors of (A) mean streamwise velocity, $\epsilon_U$, and (B) turbulence intensity, $\epsilon_I$, versus number of cells with horizontal axis in the linear and vertical axis in the logarithmic presentation

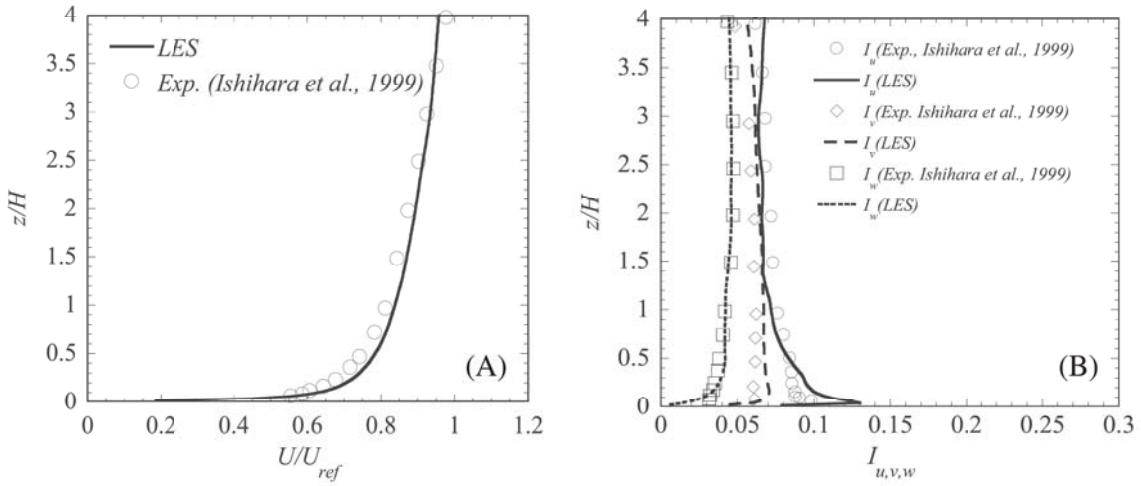


**FIGURE 6** Vertical profiles of (A) mean streamwise velocity and (B) turbulence intensity in the generated atmospheric boundary layer flow

For $U$ contours (Figures 7B and 8B), on the upwind side, $U$ exhibits an obvious accelerating trend around the hillcrest. Away from the crest, the flow separates clearly. A separation bubble can be identified between $x$ = 0.05 $L$ and $x$ = 1.1 $L$ for the 3D hill and between $x$ = 0.02 $L$ and $x$ = 2.3 $L$ for the 2D hill.

For $u$ contours (Figures 7C and 8C), the fluctuation near the summit becomes weaker when the topography is changed from a 2D hill to a 3D hill. The region with large fluctuations covers a wider region for the 2D hill, indicating a stronger mixing effect.

Mean velocity streamlines at $y$ = 0 are presented in Figures 7D and 8D. In the wake of the 3D hill, there is no recirculation zone because of the mean spanwise flow, which is discussed in detail in terms of the continuity governing equations by Ishihara et al.[35] Further, it is important that the streamlines upstream of the 2D hill are considerably steeper than those upstream of the 3D hill and that the region affected by the topography is larger for the 2D hill. This implies that the 2D hill has a stronger effect on the wind turbine wake. The streamlines starting from the center of the rotors (B-line) are also represented in Figures 7E and 8E. These streamlines are adopted for the superposition of the wind speed deficit, as discussed in Section 3.4.5.

The profiles of $U$ are shown in Figures 7B and 8B. Neglecting some small discrepancies in the hill wake region, the results for the mean velocities generally exhibit good agreement with the experimental data. From the profiles of the mean streamwise velocity in the far-wake region, we observe that the recovery of the wind speed is slower for the 2D hill than for the 3D hill. In the present study, four lines (A-line, B-line, C-line, and D-line) will be considered, which are summarized as:

- A-line: mean flow streamline of the flow fields considering both the terrain and turbine;
- B-line: mean flow streamline of the flow fields only considering the terrain;
- C-line: connection of turbine wake center at each $y$–$z$ cross section;
- D-line: line with a vertical distance of hub-height on $x$–$z$ slice.

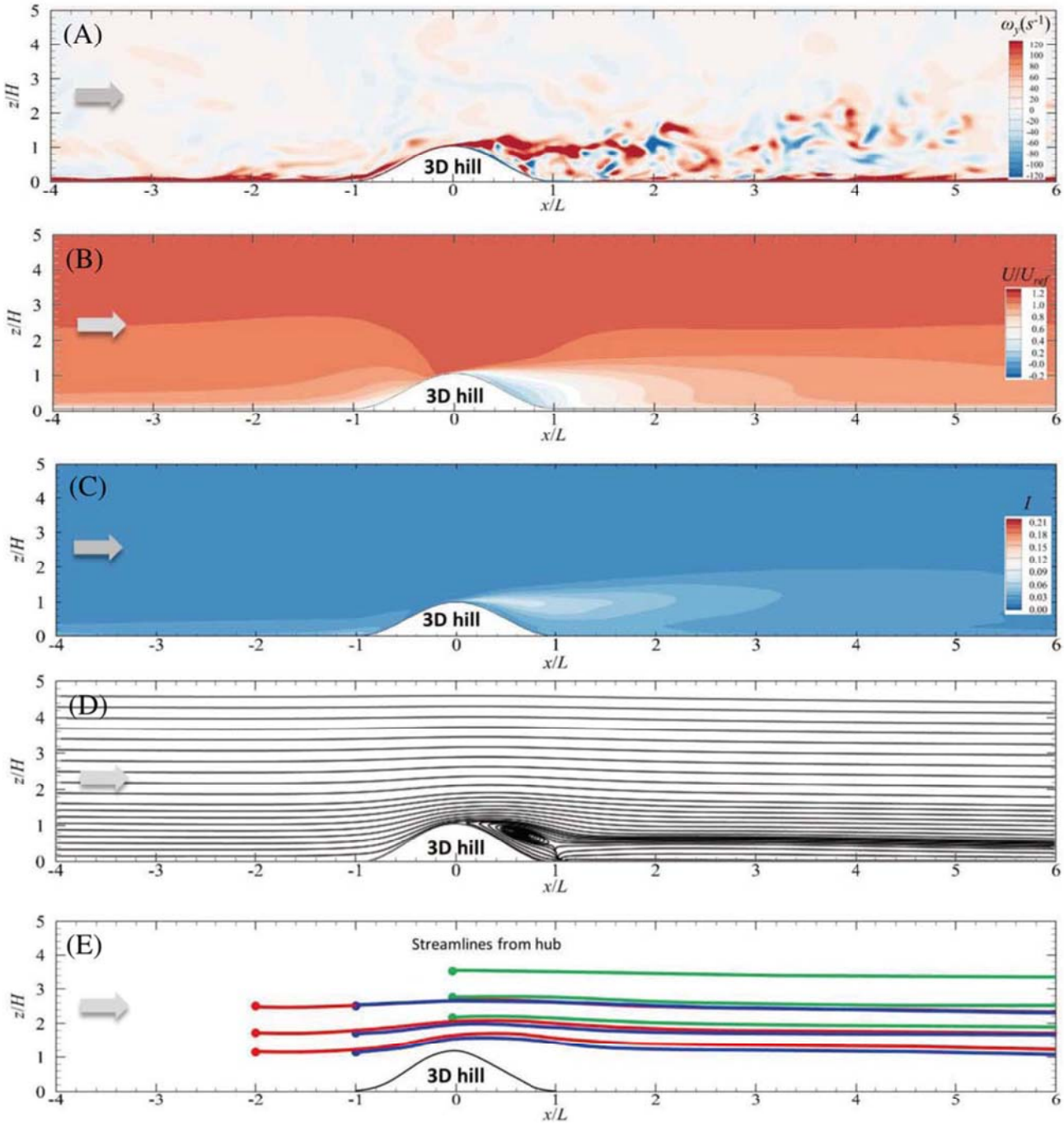


**FIGURE 7** Flow fields over a 3D hill in the absence of the wind turbine, (A) instantaneous vorticity in spanwise direction, (B) mean streamwise velocity, (C) turbulence intensity, (D) streamlines, and (E) streamlines starting from the hub height of the wind turbine, on the vertical plane $y = 0$

Vertical profiles of mean streamwise velocities at several locations from $x = -L$ to $x = 3\ L$ with a step size of $0.5\ L$ for the 3D hill are shown in Figure 9A, respectively. The profiles are normalized by $U_{ref}$. On the whole, the numerical results provide acceptable agreement with those in experiment for the mean velocity components. At the upwind side, the streamwise mean velocity shows an obvious acceleration at the crest of the hill where the vertical gradient of the streamwise mean velocity versus the height shows high value (see Figure 9A). After the crest, the flow separation could be clearly identified. The reverse point, at which the flow direction is changed from positive to negative as approaching the surface, emerges. The height of the reverse point decreases as increase the downstream distance and attaches the ground at the foot of the hill. The region of the separation bubble is identified which starts at $x = 0.9\ h$ and ends at $x = 2.5\ h$, same with the results from experiments by Ishihara et al.[36]

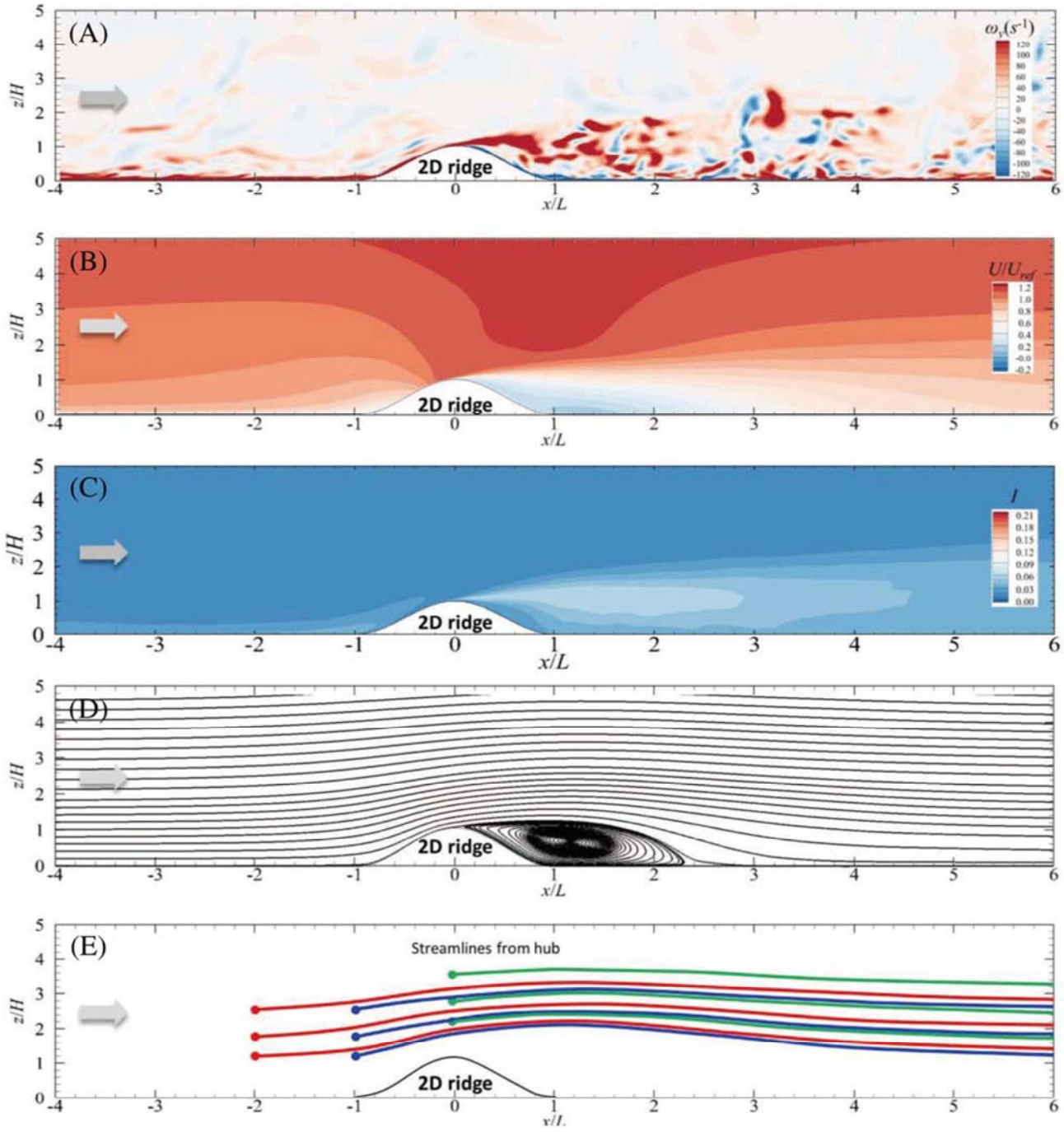


**FIGURE 8** Flow fields over a 2D hill in the absence of the wind turbine, (A) instantaneous vorticity in spanwise direction, (B) mean streamwise velocity, (C) turbulence intensity, (D) streamlines, and (E) streamlines starting from the hub height of the wind turbine, on the vertical plane $y = 0$

The profiles of mean streamwise velocity for the 2D hill, as shown in Figure 10A, are normalized and scaled in the same way as those of the 3D hill (Figure 9a) for a clearly comparison between them. The shear layer and the region of separation bubble are determined and drawn as the above presentations. Except for some little discrepancies in the wake region, the prediction of mean velocities overall provides good agreement with the experimental data. The profiles of mean streamwise velocity in the far-wake region show that the recovery of the wind speed becomes slower when the ground topography is 2D hill compared with 3D hill and separation bubble becomes larger The separation point and reattachment point locate at 1.2 and 4.7 $h$, respectively. The locations of separation point and reattachment point are close to the experimental results by Ishihara et al.[36]

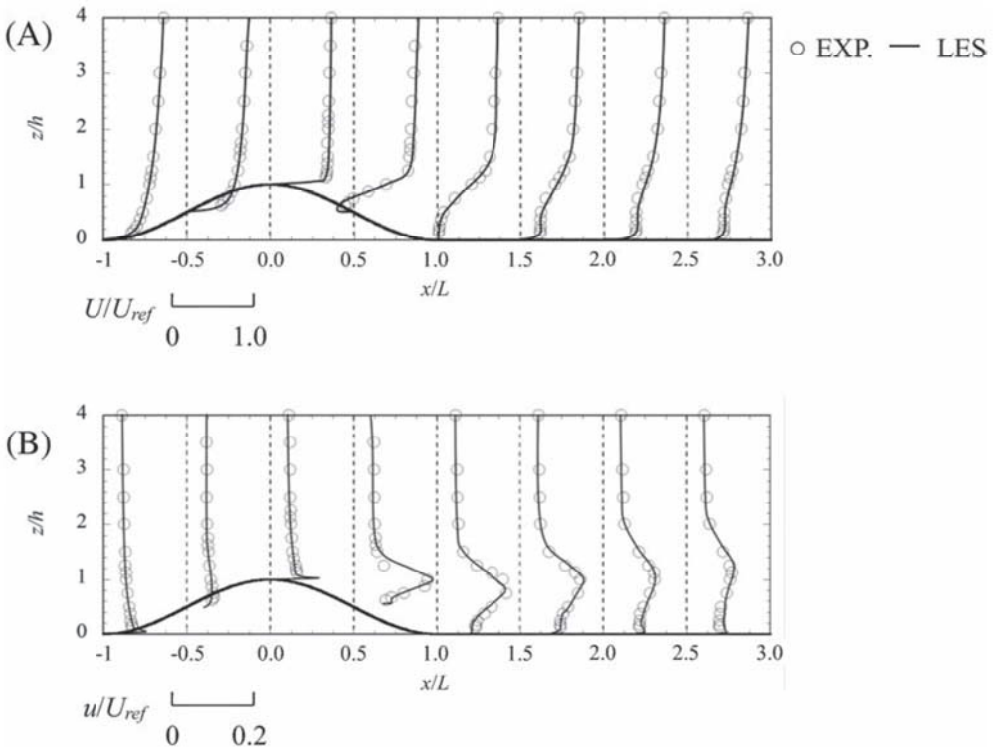


**FIGURE 9** Vertical profiles of (A) mean streamwise velocity and (B) turbulence intensity over 3D hill

In Figures 9B and 10B, the profiles of turbulence intensity $I$ and a comparison with experimental results are presented. Turbulence intensity is determined as the ratio of $u$ to $U_{ref}$; it agrees well with the experimental results. The height under which the profiles are distorted is considerably higher for the 2D hill than for the 3D hill. The magnitude of $u$ away from the wake region is larger for the 2D hill than the 3D hill. A sharp peak appears at the hill summits for $u$; this can be observed in the snaps of simulations in Cao et al.[48] and Tamura et al.,[54] but not the case in the

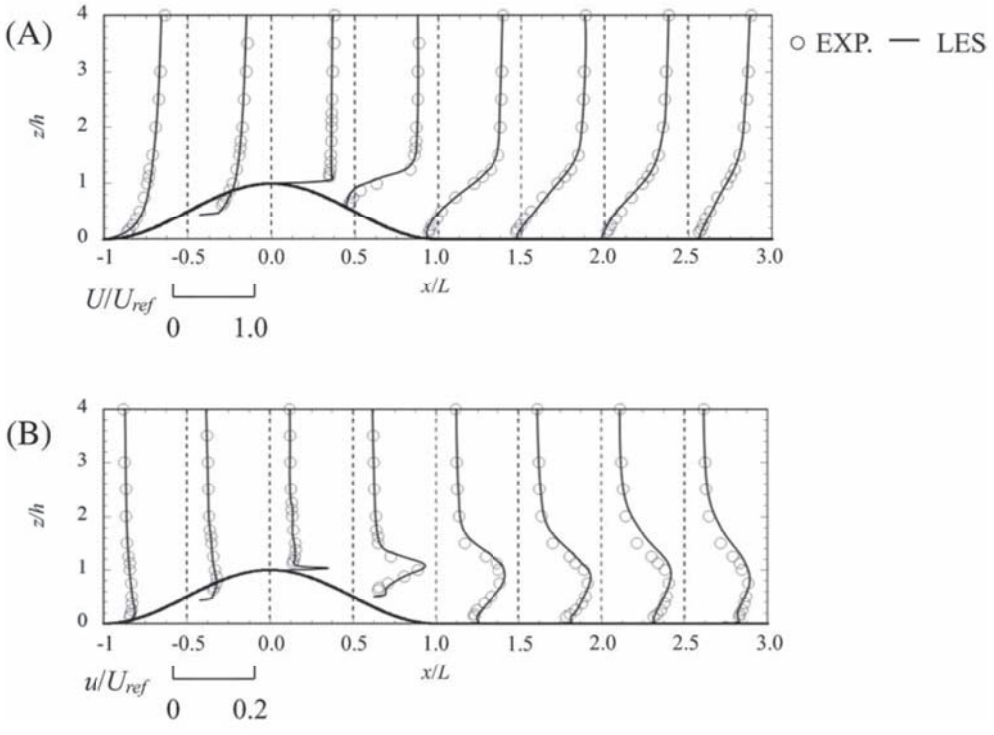


**FIGURE 10** Vertical profiles of (A) mean streamwise velocity and (B) turbulence intensity over 2D hill

experiment. The reason of the difference perhaps emerges from the different wall conditions between the numerical model and the real experimental model as well. The height under which the $I_u$ profiles are distorted in the case of 2D hill is much higher than 3D hill. The magnitude of $I_u$ in the far-wake region of 2D hill (see Figure 10B) is larger compared with the case of 3D hill, which is due to the fact that in the case of 3D hill, the flow with lower turbulence density around the wake could be transported into the wake region because of the existence of the mean spanwise flow in the wake (even it is zero at the central slice) and this low turbulence flow will mix with flow in the wake; as a result, the turbulence in the wake of 3D hill is reduced. In the case of 2D hill, the statistical flow field is not 3D but 2D, that is, the vertical distributions of the turbulence statistics do not change with the spanwise locations; therefore, the mixing of flow in the spanwise direction could not occur. Some overestimations could be found for the turbulence intensity which were also found in the study by Cao et al.[48] who applied LES turbulence model as well; therefore, further research is deserved to be carried out in the future to understand the reasons of these discrepancies.

## 3.4 | Flow interaction between typical topographies and wind turbines

In this section, the flow interaction between typical topographies and wind turbines is examined; further, the condition under which the superposition method can be adopted is clarified.

### 3.4.1 | Instantaneous vortical structures ($\omega_y$)

*Wind turbines located at* x = −2 L

Instantaneous vortical structures are illustrated by instantaneous $\omega_y$, shown in Figures 11–13, and streamlines starting from the nacelle after the introduction of the turbines (thick dashed lines, "A-line") and in the absence of the turbines (thick solid lines, "B-line") are superimposed on them. The mean flow streamlines were determined as a spatial curve drawn in the mean flow field, and on the curve, the velocity vectors of all particles are tangent to this curve. The advection of the wake center, determined by the time-averaged locations with the strongest wind deficit on the cross sections of the wake ($y$–$z$) slices, is plotted in dotted lines ("C-line"). Instantaneous $\omega_y$ in Figure 11 indicates that the wake of the turbine located at $x = -2\ L$ can be transported downstream of the 3D or 2D hills. The coupling effect between the turbine and hill is not as pronounced upstream of the hill as it is downstream of the hill. Wind speed at the hill summit and mixing effect of hill-generated vortices downstream lead to a faster wake diffusion. In addition, because of the advection of additional turbulence caused by turbines, the wake is larger in size than that in the absence of turbines.

In particular, the wake flow of turbine T1 is the most diffused, and its wake recovery is the fastest (Figure 11A,B). The thickness of the hill-induced wake is almost the same as that in the hub height of T1; thus, the mixing effect among T1 wake, ambient turbulent flow, and hill-induced wake is more pronounced. The tip vortex is no longer visible beyond the summits of the hills for T1, whereas for T3, the tip vortex can extend even to the region 4.2 $D$ downstream of the hills (Figure 10C,F), thereby indicating a weaker interaction between the turbine-induced and hill-induced wakes as the turbine size increases. Vortices generated by turbine T1 are approximately the same size as the hill vortices (Figure 11A, D). As the size of the turbine increases, the size of the vortices created by it increases accordingly. For turbines T2 (Figure 11B,E) and T3 (Figure 11C,F), there is a significant difference in scale between the hill-induced and turbine-induced vortices, which is another probable reason for their weak interaction when the aspect ratio $h/H$ is high.

The vertical deflection of tip vortex over the 2D hill seems to follow the curvature of the topography (Figure 11d–f), while for the 3D hill, the vertical deflection shows less pronounced inclination from $x = -L$ to $x = 0\ L$ (Figure 11A–C). This is attributed to the fact that when the terrain is a 3D hill, the turbine-induced wake can flow around freely through the lateral sides of the hill, while for a 2D hill, there is no such passage, which leads to a stronger elevating effect on the windward side of the 2D hill.

*Wind turbine located at* x = −1 L

When turbines are located 1 $L$ upstream of the hills, flow patterns maintain the major features observed when the turbines are located at $x = -2\ L$, such as the inclination of tip vortices over the windward side of the hills, as shown in Figure 12. Compared to Figure 11, the inclination of the wake is more evident. Furthermore, the discrepancy between the streamline over the hill and the wake center is more evident in the absence of the turbine, and this may be a sign of a stronger interaction. Further, we can see that the region with energetic vortices covers a larger area compared to the counterparts with the turbines located at $x = -2\ L$; therefore, it may be difficult to apply superposition to predict the wind speed deficit when the turbine is located at the upstream foot of a hill.

*Wind turbine located at* x = 0 L

When wind farms are constructed in complex terrains, wind turbines are located at the terrain top; therefore, it is important to examine interactions between the summit-mounted turbine and the terrain. Instantaneous vorticities in this scenario are shown in Figure 13. When the turbine

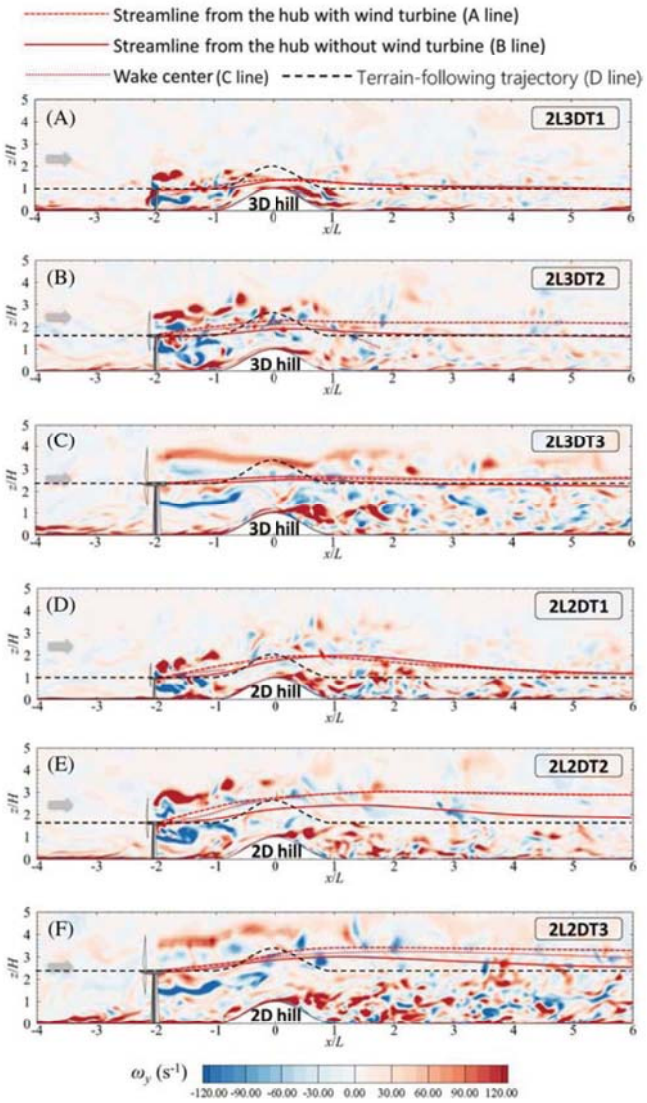


**FIGURE 11** Instantaneous vorticity on the vertical plane $y = 0$ for (A) 2L3DT1, (A) 2L3DT2, (C) 2L3DT3, (D) 2L2DT1, (E) 2L2DT2, and (F) 2L3DT3. Mean flow streamlines from the wind turbine hub with wind turbine (A-line) illustrated by dashed lines, those without wind turbine (B-line) illustrated by solid lines, and the locations of the wake center (C-line) illustrated by dotted lines are superimposed

size is small (T1), the wind turbine and hill act together as a single obstacle (Figure 13A,D), and there is no obvious boundary between the turbine- and hill-induced wakes; this indicates the almost full coupling effects. As evident in Figures 12D and 13A, after the introduction of the wind turbine on the summit, the vortices in the flow downstream of the turbine become larger and exhibit a type of wavy shedding. The shedding frequency is related to the wind speed, hill height, and turbine size. The shedding effects induce fast recovery of the wake flow, which is observed again in the distribution of $U$. As the turbine size increases, wavy shedding becomes less obvious. In the case of T3 (Figure 13C,F), clear tip vortices emerge again.

### 3.4.2 | Mean streamwise velocity ($U$)

*Wind turbines located at* x = −2 L

Figure 14 shows the distribution of $U$ normalized by $U_{ref}$ on the $y = 0$ plane when the wind turbines are at $x = -2$ L. It is once more evident that with increased turbine size (T3), the deficit of the wind speed can extend even to 8 $D$ downstream of the turbine (Figure 14C,F). In contrast, for turbine T1 (Figure 14A,D), the deficit is almost completely diffused at the upstream foot of the hills. The wind speed-up $\Delta S$, which is an important parameter for evaluating wind resource, is defined as $\Delta S = \Delta U/U_0 = [U(x,z') - U_0(z')]/U_0(z')$, where $U(x,z')$ denotes the streamwise velocity at height $z'$ and $U_0(z')$ is the reference streamwise velocity at the same height in the absence of the topography and the turbine. It is interesting and important that there exists a region characterized by extraordinarily high wind speed-up ($\Delta S \approx 1.2$), located in the layer between the turbine wake and the hill summit. Wind passing the wind turbine should decelerate due to drag effects; however, according to the mass conservation law, the flow near the outside boundary of the wind turbine wake accelerates, and it is further accelerated by the curved shape of the topographies. Owing to

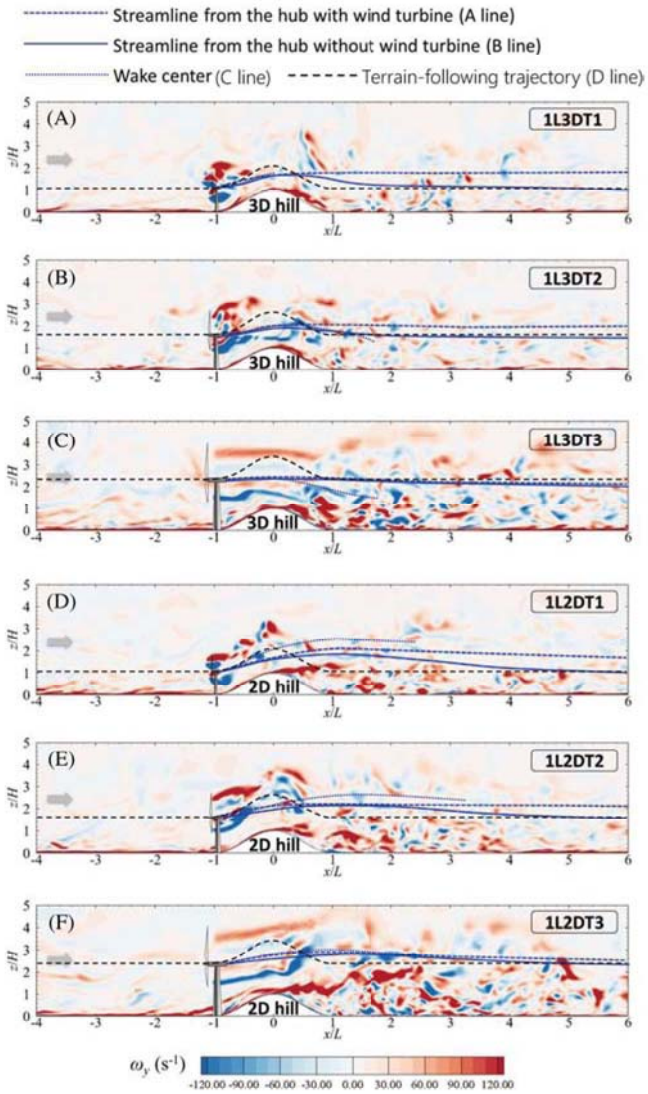


**FIGURE 12** Instantaneous vorticity on the vertical plane $y = 0$ for (A) 1L3DT1, (B) 1L3DT2, (C) 1L3DT3, (D) 1L2DT1, (E) 1L2DT2, and (F) 1L3DT3. Mean flow streamlines from the wind turbine hub with wind turbine (A-line) illustrated by dashed lines, those without wind turbine (B-line) illustrated by solid lines, and the locations of the wake center (C-line) illustrated by dotted lines are superimposed

the relatively smaller diffusion effect and the relatively shorter distance to hill for the larger turbine, the acceleration around the wake is more pronounced as $h/H$ increases. For turbine T3 (Figure 14C,F), the region with high acceleration around the wake can even touch the hill summit, thereby generating more evident wind speed-up than for turbines T1 (Figure 14A,D) and T2 (Figure 14B,E). In addition, when compared with the 3D hill (Figure 14A–C), stronger wind speed-up at the summit caused by the coupling of the wind turbine and the hill can be observed for the 2D hill (Figure 14D–F). Further, this can be explained by the mass conservation law of the fluid. For the 2D hill, there is no passage for the fluid on the lateral sides as in the 3D hill, and the accelerated fluid around the turbine wake can only flow following the curved shape of the 2D hill. This means that the area for the flow to pass the 2D hill is smaller than that for the 3D hill. Consequently, the wind acceleration at the summit of the 2D hill is 1.2 times as strong as the 3D hill. This finding is important for the optimization of wind farms that use turbines with different hub heights in complex topographies. The velocity magnitudes at the rotor are different for the three turbines. It is because that the ambient velocities are low at the low elevation, but the decreased ratio of the velocity magnitude due to the drag of the wind turbine is close. The different velocity magnitude may also due to the interaction between the turbine wake and the ground, because the turbulence characteristics over the ground are different at different height.

Discrepancy between Lines A and C is evident for the 2D hill. This is an indication of the stronger interaction between the 2D hill and the turbine wake. Further, it indicates that for the 2D hill, it is more difficult to determine the wake center using only the flow fields in the absence of the wind turbine. However, when the aspect ratio $h/H$ is sufficiently large and the topography is a 3D hill (i.e., T3 over the 3D hill; Figure 14C), Lines A and C are in nearly the same location, thereby implying that it is possible to determine the wake center using only the information about the flow fields over the topography without the turbine and predict the wake flow by applying the superposition method. This is important for optimizing wind farms in complex terrain using the analytical turbine wake model and genetic algorithm (GA).

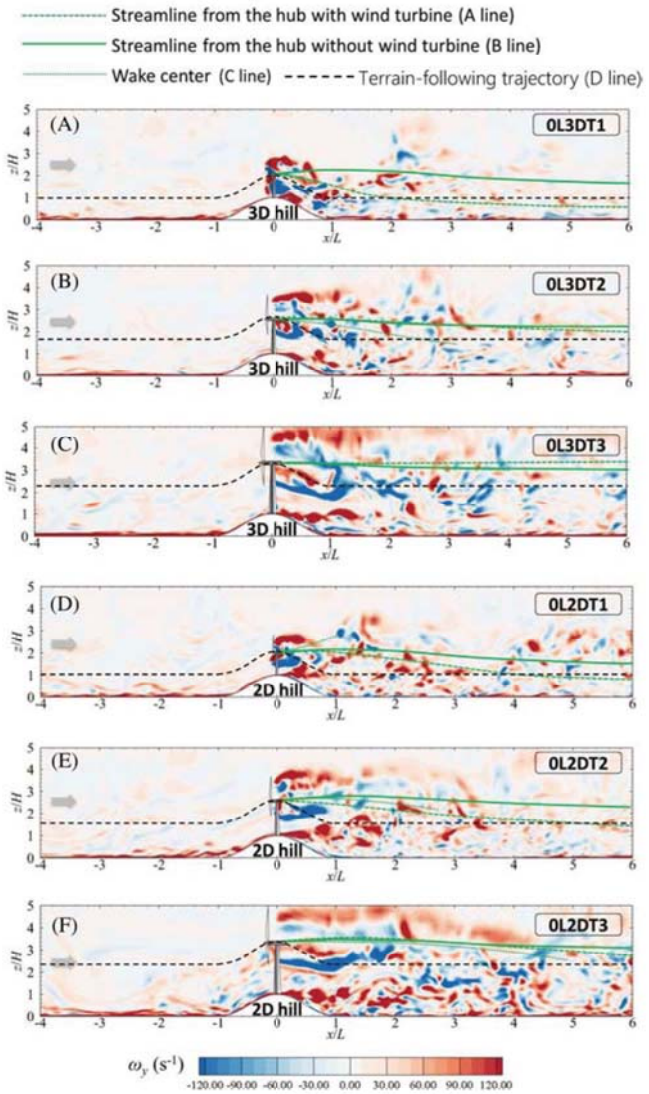


**FIGURE 13** Instantaneous vorticity on the vertical plane $y = 0$ for (A) 0L3DT1, (B) 0L3DT2, (C) 0L3DT3, (D) 0L2DT1, (E) 0L2DT2, and (F) 0L3DT3. Mean flow streamlines from the wind turbine hub with wind turbine (A-line) illustrated by dashed lines, those without wind turbine (B-line) illustrated by solid lines, and the locations of the wake center (C-line) illustrated by dotted lines are superimposed

*Wind turbines located at* x = −1 L

The contours of $U$ for the cases with the turbine located at $x = -1$ $L$ are shown in Figure 15. Reducing the distance between the wind turbine and topographies can significantly accelerate the flow in between the turbine wake and the hill summit. The most evident increase in wind speed-up ($\Delta S = 1.22$) is found for turbine T1 (Figure 15A,D). Even though the acceleration of the flow near the hill summit is stronger as the distance decreases, the region of the flow with high speed-up is compressed to a thinner layer than for the cases 2 $L$ upstream of the hill (Figure 15). Owing to this strong jet, it is more difficult to reattach the flow to the ground; therefore, the recirculation bubble behind the hill is stretched, and the wind speed in the bubble is weakened. After the 3D hill summit, the turbine wake shows an apparent downward inclination, which is not observed for the 2D hill. This is probably because of the stronger jet flow near the 2D hill summit, which maintains the center of the turbine wake as a nearly horizontal line. Further, it can be observed that decreasing the distance between the hill and the topographies makes it considerably easier for the turbine-induced wake to mix with the hill-induced wake. For example, the apparent mixture of the wakes starts from $x = 2$ $L$ for turbine T3 located 1 $L$ upstream of the 3D hill (Figure 15C); in contrast, when turbine T3 is located 2 $L$ upstream of the 3D hill (Figure 14C), the separation of the turbine- and hill-induced wakes is clear.

*Wind turbines located at* x = 0 L

For turbine T1, the height of the wake center is much lower than the height of Line A, as shown in Figure 16A,D. This is attributed to the abruptly full coupling effect between the turbine and the hill. For larger wind turbines, the difference between the wake center and Line A is less evident, and when mounted at 0 $L$, the separation between the turbine- and hill-induced wakes is much clearer than that when mounted 1 $L$ upstream. Furthermore, in contrast to the cases with the turbine mounted 2 $L$ and 1 $L$ upstream of the hill (Figures 14 and 15), at 0 $L$, there is almost no upward motion of the accelerated flow near the hill summit.

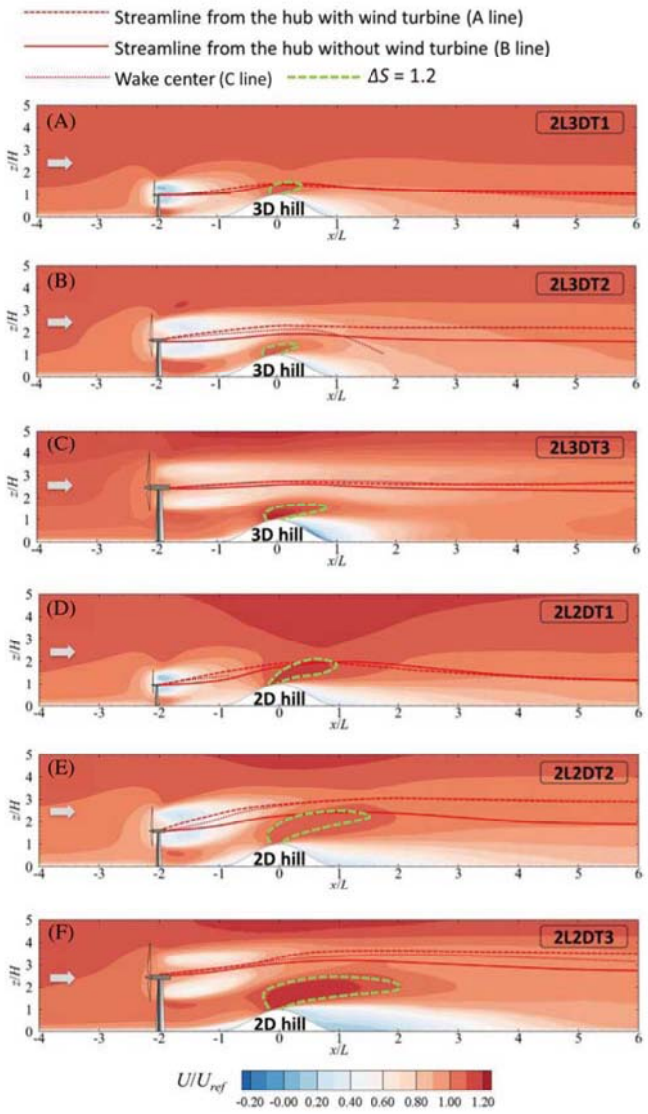


**FIGURE 14** Mean streamwise velocity on the vertical plane y = 0: (A) 2L3DT1, (B) 2L3DT2, (C) 2L3DT3, (D) 2L2DT1, (E) 2L2DT2, and (F) 2L3DT3. Mean flow streamlines from the wind turbine hub with wind turbine (A-line) illustrated by dashed lines, those without wind turbine (B-line) illustrated by solid lines, and the locations of the wake center (C-line) illustrated by dotted lines are superimposed

### 3.4.3 | Streamwise turbulence intensity (*I*)

While mean streamwise velocity is important to predict wind energy and to optimize the wind farm, turbulence intensity is a critical parameter for determining the fatigue loads of wind turbines[55–57] and the key parameter for modeling wake recovery.[34,58,59] Thus, it is meaningful to provide information about turbulence intensities.

*Wind turbines located at* x = −2 L

The contour of *I* is shown in Figure 17, with streamlines starting from the rotor center without the wind turbines and the locations of the turbine wake center superimposed. At the upstream foot of the hills, the horseshoe vortex caused by the blocking effects of the topographies is enhanced by the introduction of the turbines. This horseshoe vortex is very close to the ground; therefore, the interaction with the turbine wake is clear only for low turbines (T1 and T2). This interaction seems increasing the vorticity of the turbine wake flow, as can be seen in Figures 11, 12, and 13 about the vorticity of the flow on *x*–*z* slice. The turbulence intensity downstream of the hills is intensified when the wind turbines are mounted upstream. This effect is more pronounced as wind turbine size increases or when changing the shape of the topography from 3D to 2D hill. For the case 2L2DT3 (Figure 17F), both the height and length of the region with *I* = 15% are almost doubled similar to those in the absence of turbines (Figure 10). The enhancement of the turbulence in the hill wake is likely caused by two factors: the additional turbulence from the wind turbine wake and the higher energetic flow acceleration near the hill summit after the introduction of the wind turbines, which can cause stronger flow separation and transport the generated turbulence to a location further downstream.

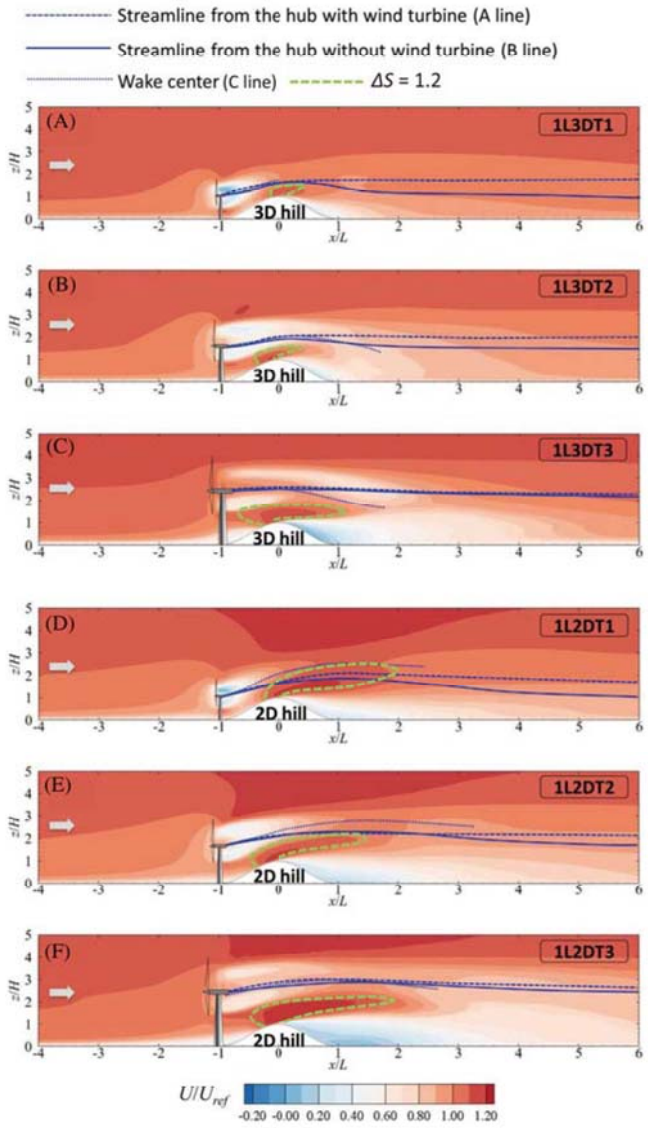


**FIGURE 15** Mean streamwise velocity on the vertical plane $y = 0$: (A) 1L3DT1, (B) 1L3DT2, (C) 1L3DT3, (D) 1L2DT1, (E) 1L2DT2, and (F) 1L3DT3. Mean flow streamlines from the wind turbine hub with wind turbine (A-line) illustrated by dashed lines, those without wind turbine (B-line) illustrated by solid lines, and the locations of the wake center (C-line) illustrated by dotted lines are superimposed

*Wind turbines located at* x = −1 L

Figure 18 shows the turbulence intensity when the wind turbine is located 1 *L* upstream. It is evident that compared with the cases when the turbines are 2 *L* upstream from the topographies, the coupling effects are more obvious and the turbulence in the hill wakes is intensified in terms of both the magnitude and the area.

*Wind turbines located at* x = 0 L

From the contours of the turbulence intensity, the mixture of wakes for turbine T1 mounted at the hill summits is obvious, as seen in Figure 19A,D. In the near-wake region, the wake caused by the disturbance of turbine T1 and that caused by the hill are almost fully merged. High turbulence intensity that occurs in the recirculation bubble in the absence of the wind turbine disappears, leaving a relatively quiet area on the leeside of the hills. This feature is also observed for turbine T2 on the 2D hill (Figure 19E). As the wind turbine size increases, the region with high turbulence intensity near the leeside of the hills appears again.

### 3.4.4 | Superposition method examination for mean streamwise velocity

To clarify the conditions under which the superposition method can be adopted, profiles downstream from wind turbines with distances 0.5 *L*, 1.0 *L*, …, 4.0 *L* are plotted in Figures 20–22, where the results from the simple superposition method are also drawn. In the superposition method, the wake deficit obtained from the turbines mounted on a flat ground is superposed following Line B (brown dashed line) and Line D (blue dashed line).

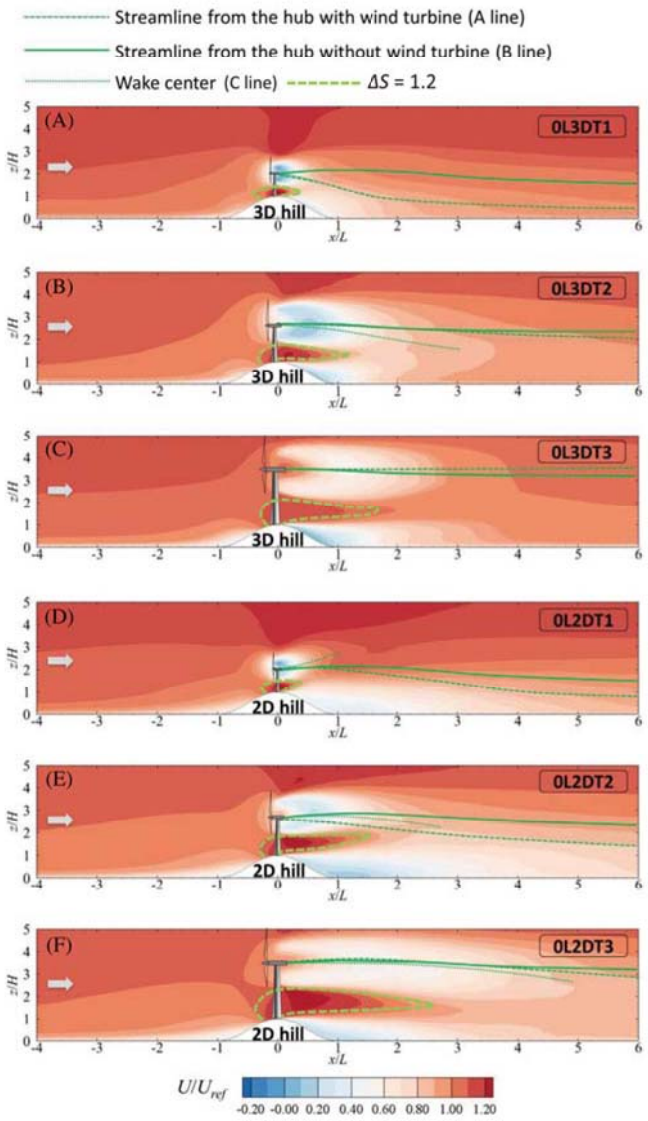


**FIGURE 16** Mean streamwise velocity on the vertical plane y = 0: (A) 0L3DT1, (B) 0L3DT2, (C) 0L3DT3, (D) 0L2DT1, (E) 0L2DT2, and (F) 0L3DT3. Mean flow streamlines from the wind turbine hub with wind turbine (A-line) illustrated by dashed lines, those without wind turbine (B-line) illustrated by solid lines, and the locations of the wake center (C-line) illustrated by dotted lines are superimposed

These two lines were chosen to test the superposition method because Line B is close to the real center of the wind deficit, thereby making it possible to reproduce the turbine wake flow over topographies successfully, while Line D is the location where the wind deficit is added in most wake models in complex topographies.[16,60] The relative errors of the superposition methods are plotted as bars at the top of each profile; the relative errors are determined as

$$\epsilon_{U_B} = \frac{\int_{z'=0}^{z'=5H} |U_H - U_B| \, dz'}{\int_{z'=0}^{z'=5H} |U_H - U_W| dz'} \tag{5}$$

$$\epsilon_{U_D} = \frac{\int_{z'=0}^{z'=5H} |U_H - U_D| \, dz'}{\int_{z'=0}^{z'=5H} |U_H - U_W| dz'} \tag{6}$$

where $U_H$ is the mean streamwise velocity considering both the hill and the turbine in the simulations; $U_B$ is the mean streamwise velocity predicted using the superposition method with the wake center following Line B; $U_D$ is the mean streamwise velocity predicted using the superposition method with the wake center following Line D; $U_W$ is the mean streamwise velocity in the absence of wind turbine; $\epsilon_{U_B}$ is the relative error of the B-line superposition method; and $\epsilon_{U_D}$ is the relative error of the D-line superposition method. All plotted relative errors using bars are in the same scale.

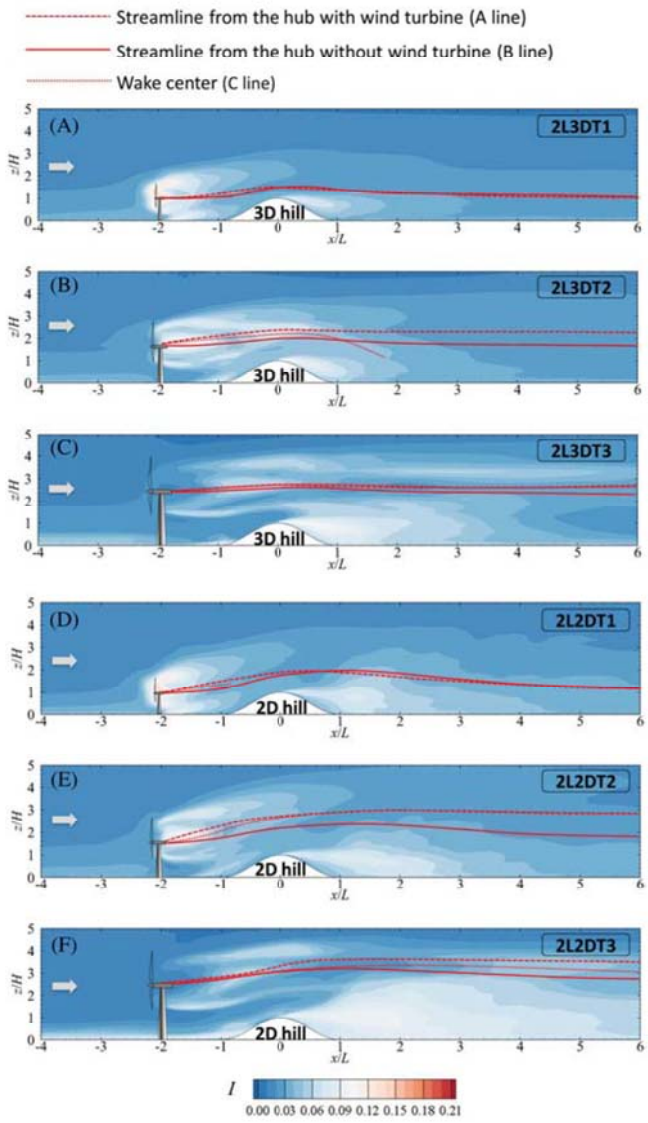


**FIGURE 17** Turbulence intensity on the vertical plane $y = 0$: (A) 2L3DT1, (B) 2L3DT2, (C) 2L3DT3, (D) 2L2DT1, (E) 2L2DT2, and (F) 2L3DT3. Mean flow streamlines from the wind turbine hub with wind turbine (A-line) illustrated by dashed lines, those without wind turbine (B-line) illustrated by solid lines, and the locations of the wake center (C-line) illustrated by dotted lines are superimposed

*Wind turbines located at* x = −2 L

It is evident that hill-generated turbulence diffuses the wake deficit, as shown in Figure 20. The relatively sharp decrease in wind speed at the boundary of the turbine-induced wake is greatly smoothed, and this smoothing effect weakens as wind turbine size increases. When the small turbines (T1 and T2) interact with the hills, the flow caused by the disturbance of the hills recovers considerably faster, exhibiting a smaller vertical gradient than that caused by only the hills. This is not the case, however, for the T3 turbine, whose wake effects can propagate to the region beyond $x = 2.0\ L$ and for which the mean streamwise velocity close to the ground shows almost the same distribution as that caused by only the terrain. The implication is that the wake effects caused by the turbine and the terrain may be considered separately, and there is a possibility of applying the superposition method.

For $\epsilon_{U_B}$ and $\epsilon_{U_D}$, the B-line method performs better than the D-line method. The error is dominant in the region downstream of the hills, especially in the hill wake region ($0.0\ L < x < 2.0\ L$); it can even reach over 60% for turbine T1 at $x = 0.0\ L$. The smallest error is for 2L3DT3, as shown in Figure 20C. For 2L3DT3, the error of the B-line method is less than 15% even in the near-wake region. Moreover, for 2L3DT3, the improvement of the B-line method relative to the D-line method is the most obvious. Nevertheless, owing to the faster recovery of the T3 wake over the 2D hill caused by the stronger turbulence in the hill wake and more evident interactions (Figure 20F), both the B-line and D-line methods perform poorly in predicting the T3 wake flow in the region downstream of the 2D hill. The relative error is about 30%, which is still considerably less than the errors for turbines T1 and T2, whose value in the far-wake region $x > 2\ L$ is over 60%. Considering the applicability of the superposition method for predicting $U$, we can therefore conclude that when the wind turbine is mounted 2 $L$ upstream of the hills, only the B-line method can be adopted and applied for wind turbines with hub heights no less than 2.5 times the hill height. Notably, for 3D hill, B-line method performs worse than D-line method at the locations just downstream the hill for the turbines T1 and T2. And for 2D hill, B-line method performs worse than D-line method at the hilltop.

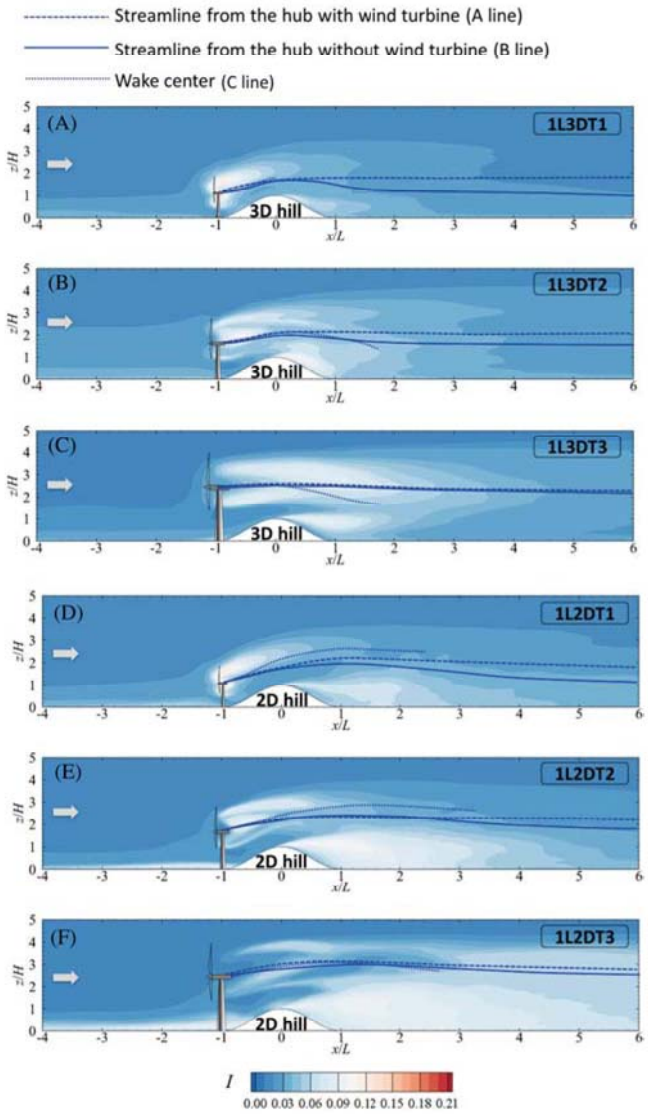


**FIGURE 18** Turbulence intensity on the vertical plane $y = 0$: (A) 1L3DT1, (B) 1L3DT2, (C) 1L3DT3, (D) 1L2DT1, (E) 1L2DT2, and (F) 1L3DT3. Mean flow streamlines from the wind turbine hub with wind turbine (A-line) illustrated by dashed lines, those without wind turbine (B-line) illustrated by solid lines, and the locations of the wake center (C-line) illustrated by dotted lines are superimposed

*Wind turbines located at* x = −1 L

The wind turbine wake center is still well predicted by the streamlines starting from the nacelle, as shown in Figure 21; however, because of the strong mixture of the wake flow downstream from the hill, the superposition method greatly overestimates the wind deficit. At $x = 3.0\ L$, the overestimation of the B-line method in 1L3DT3 reaches 62% (Figure 21C). For 1L2DT3 (Figure 21F) as presented above, there is a relatively clear separation between the turbine-induced wake and the hill-induced wake, with the result that the superposition method performs even better; the averaged $\epsilon_{U_B}$ downstream from the wind turbine is about 25%. However, the performance of B-line method is worse than D-line method in the near-wake region of turbine T1.

*Wind turbines located at* x = 0 L

The fast recovery of the wake flow for turbine T1 can be clearly identified from the plot of $U$ profiles, shown in Figure 22A,D; the profiles with and without the wind turbine are almost identical at the locations beyond $x > 3.0\ L$. For turbine T3 (Figure 22C,F), there is no apparent boundary in the turbine-induced wake, and it shows a smooth decrease of the wind speed closer to the wake center. In addition, even B-line method performs better than D-line method at all the locations, the superposition method shows large discrepancies ($\epsilon_{U_B} > 30\%$) with the simulated results for all cases at $x > 1.0\ L$, which indicates the failure of this method when the wind turbine is mounted on the hill summit.

### 3.4.5 | Summary of superposition method

Based on the examination of the two superposition methods, it is clear that only the B-line method can provide satisfactory predictions in scenarios; therefore, in this section, the overall performance of the B-line superposition method is investigated. The global difference between B-line

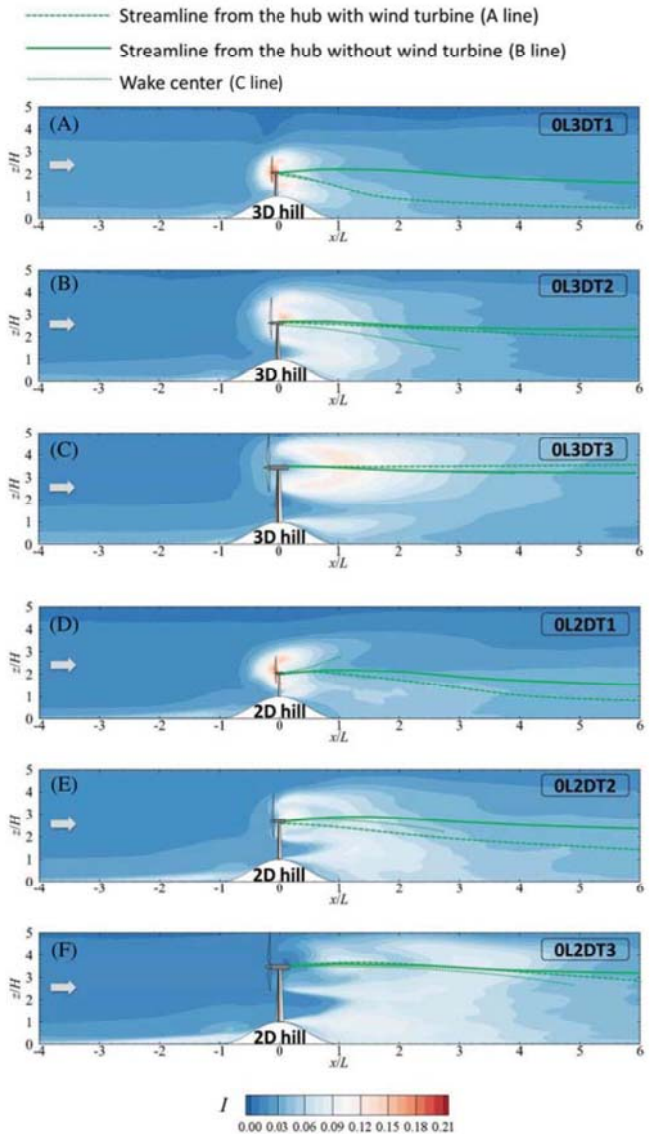


**FIGURE 19** Turbulence intensity on the vertical plane $y = 0$: (A) 0L3DT1, (B) 0L3DT2, (C) 0L3DT3, (D) 0L2DT1, (E) 0L2DT2, and (F) 0L3DT3. Mean flow streamlines from the wind turbine hub with wind turbine (A-line) illustrated by dashed lines, those without wind turbine (B-line) illustrated by solid lines, and the locations of the wake center (C-line) illustrated by dotted lines are superimposed

and wake center, $\epsilon_S$, and the global difference between the mean streamwise velocity based on B-line superposition method and the directly simulated mean streamwise velocity, $\epsilon_{GB}$, are, respectively, determined as

$$\epsilon_S = \frac{\int_{x'=0L}^{x'=L} |z'_B - z'_W| \, dx'}{\int_{x'=0L}^{x'=4L} |z'_W| \, dx'} \tag{7}$$

$$\epsilon_{GB} = \frac{\int_{x'=0L}^{x'=4L} \int_{z'=0}^{z'=5H} |U_H - U_B| \, dz'dx'}{\int_{x'=0L}^{x'=4L} \int_{z'=0}^{z'=5H} |U_H - U_W| \, dz'dx'} \tag{8}$$

Parameter $\epsilon_S$ is shown in Figure 23A. The general trend is that increasing the ratio $h/H$ or altering the hill shape from 2D to 3D hill reduces $\epsilon_S$ and $\epsilon_{GB}$. The smallest differences occur for case 2L3DT3, where $\epsilon_S$ = 1.8% and $\epsilon_{GB}$ = 12%, and the largest ones for case 0L2DT1, where $\epsilon_S$ = 19% and $\epsilon_{GB}$ = 61%. In addition, when $\epsilon_S$ is small, $\epsilon_{GB}$ also tends to be small. For any optimization of turbine layout in an onshore wind farm, we have to firstly obtain the flow fields over the terrain. After obtaining the flow fields over the terrain, we can superpose analytical wake model (without considering the terrain effects) on the obtained flow fields over terrain. From the above analysis, we can find that the location to do the superposition is a crucial factor. In addition, when using the simple B-line superposition method, the predicted mean streamwise velocity is below 20% only when $h/H$ is larger than 2.5 and the distance between the wind turbine and the hill is larger than 1 $L$. At $x = 0$, the superposition based on B-line fails, and the errors reaches more than 35%.

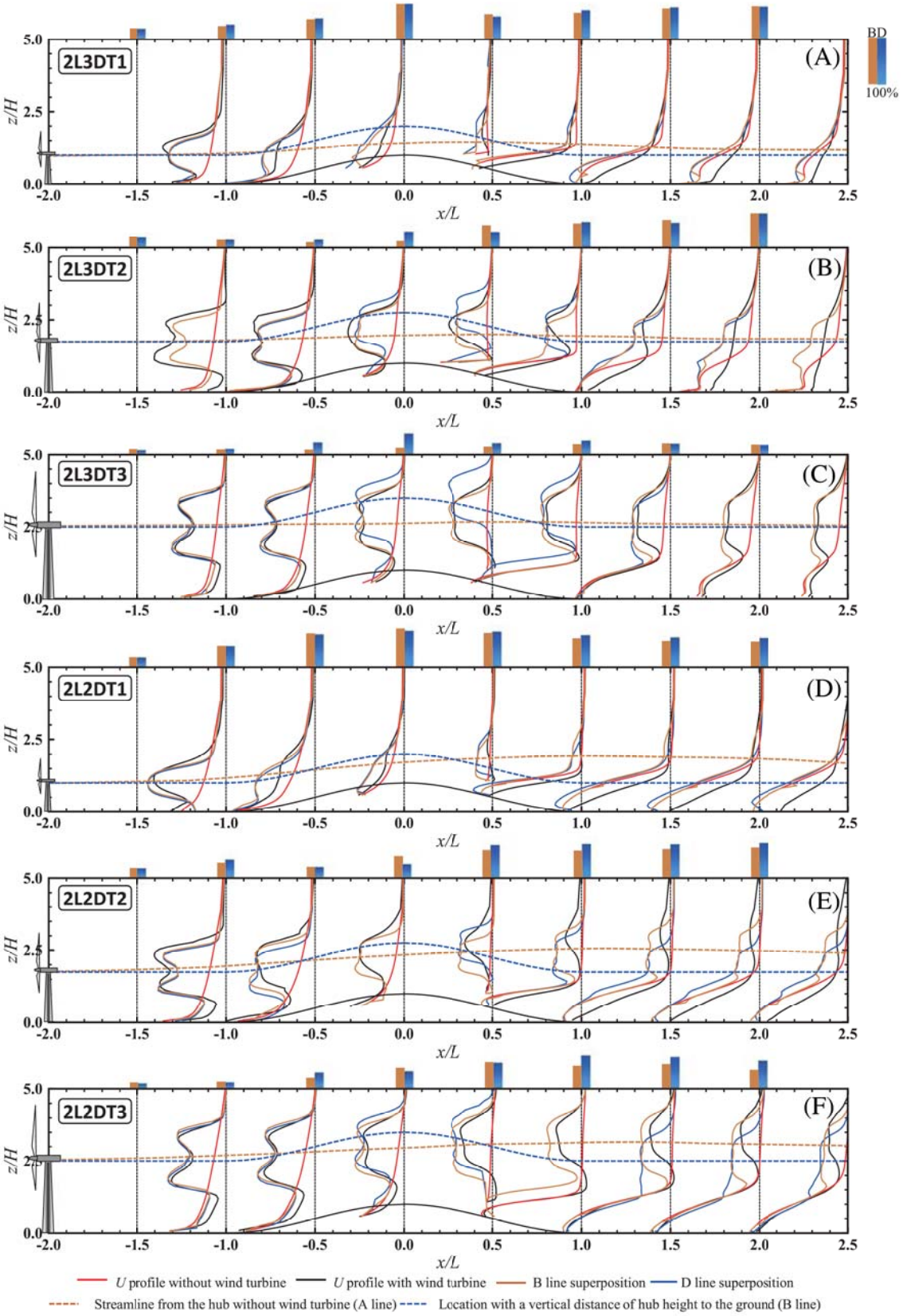


**FIGURE 20** Vertical profiles of mean streamwise velocity on the vertical plane $y = 0$: (A) 2L3DT1, (B) 2L3DT2, (C) 2L3DT3, (D) 2L2DT1, (E) 2L2DT2, and (F) 2L3DT3

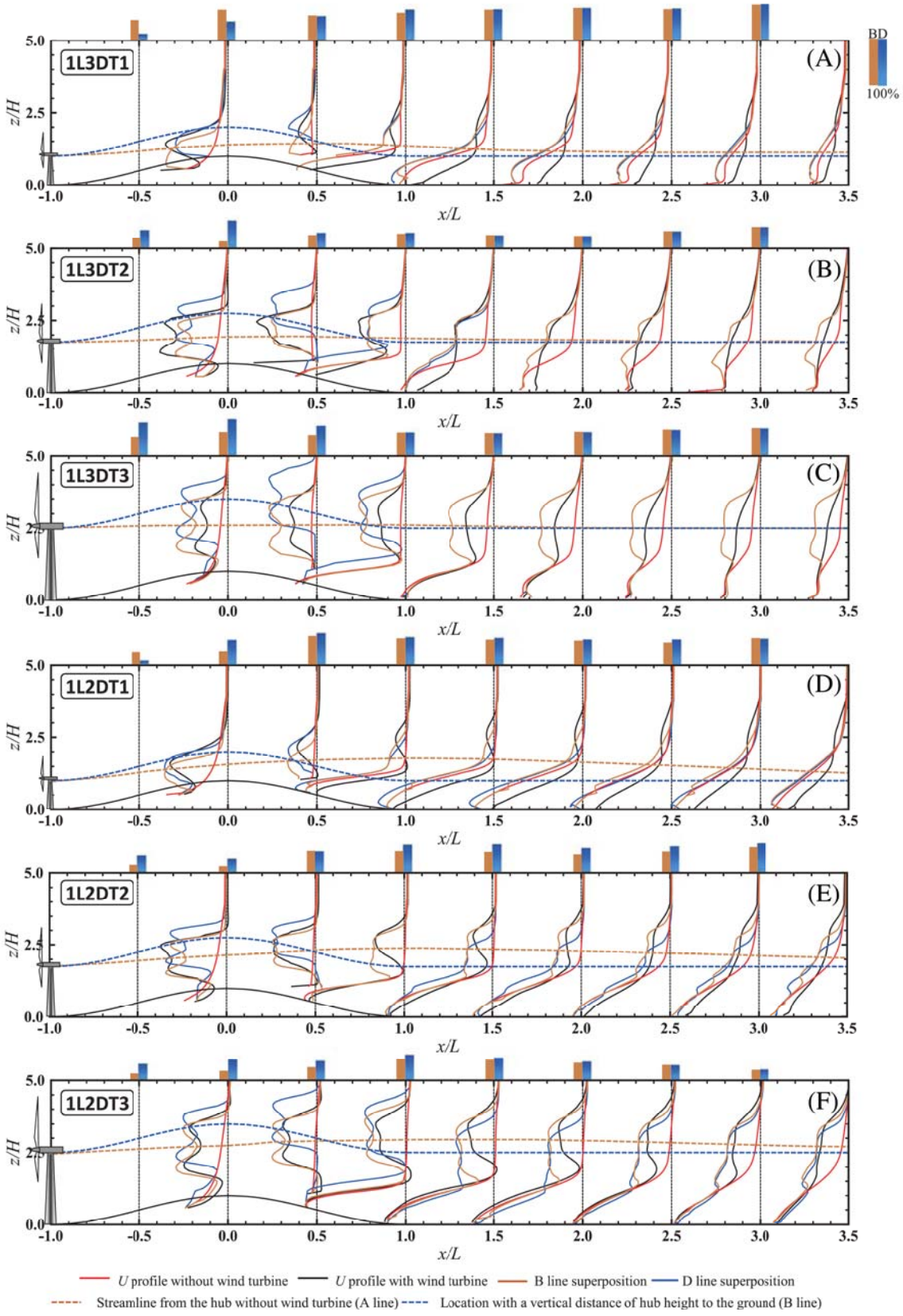


**FIGURE 21** Vertical profiles of mean streamwise velocity on the vertical plane $y = 0$: (A) 1L3DT1, (B) 1L3DT2, (C) 1L3DT3, (D) 1L2DT1, (E) 1L2DT2, and (F) 1L3DT3

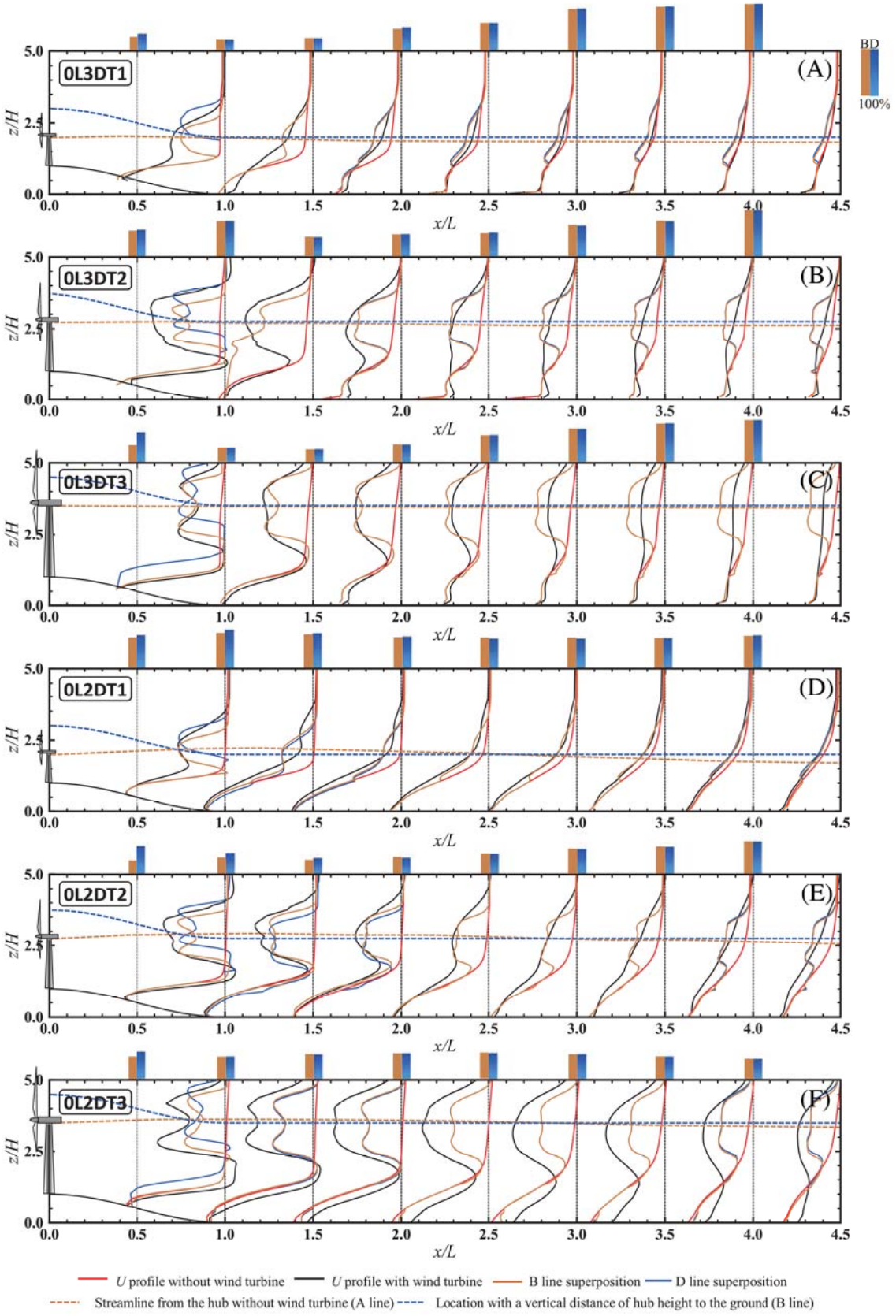


**FIGURE 22** Vertical profiles of mean streamwise velocity on the vertical plane $y = 0$: (A) 0L3DT1, (B) 0L3DT2, (C) 0L3DT3, (D) 0L2DT1, (E) 0L2DT2, and (F) 0L3DT3

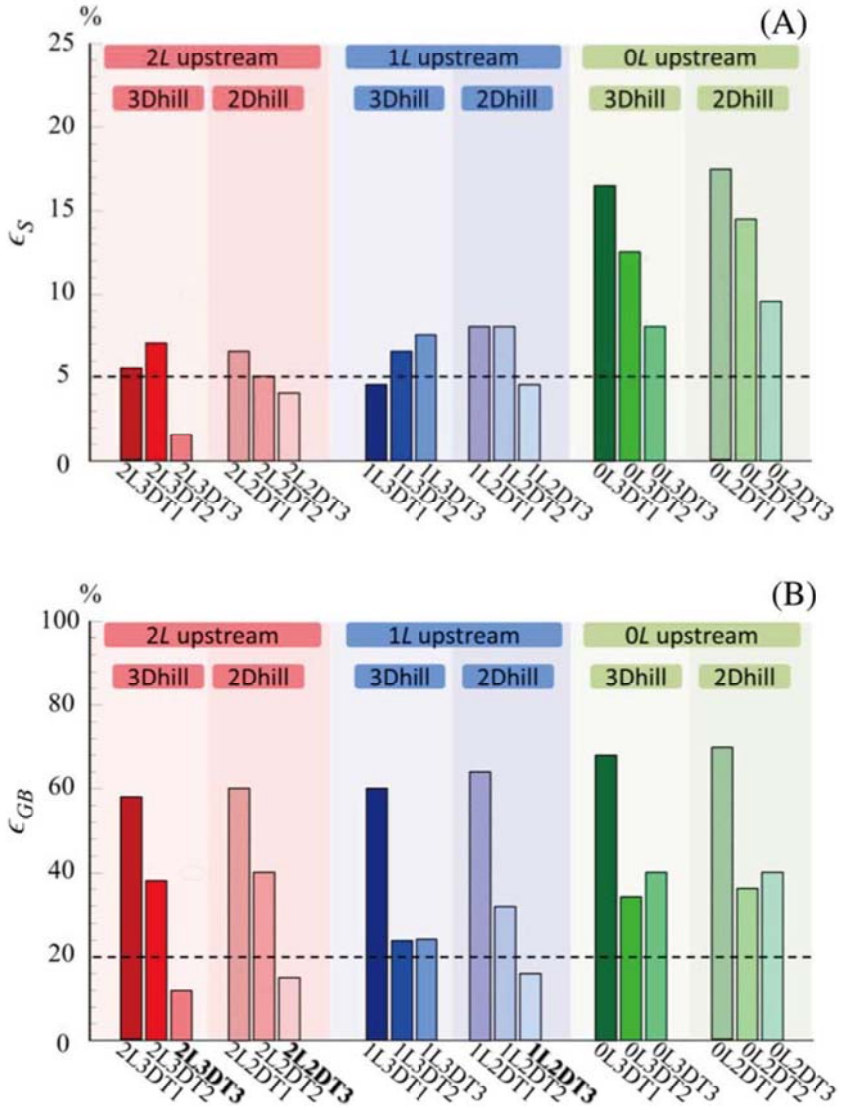


**FIGURE 23** Relative errors of the B-line superposition method. (A) Difference between the wake center and B-line and (B) difference between the flow fields by B-line superposition method and the modeled flow fields

## 4 | CONCLUSIONS

In the present study, the effects of hill shapes on the interaction between the turbine wake and the hill wake are revealed. The performance of two superposition methods is evaluated, and the condition under which the superposition method can be adopted is examined. The following conclusions can be drawn from the findings in this study:

1. When the ratio of the height of the wind turbine to the height of hill, $h/H$, is smaller than 1, the turbine-induced vortices interact strongly with the near-ground vortices in the ambient turbulence flow and hill-induced vortices. Consequently, the separation between turbine wake and the hill wake is unclear. For $h/H > 2$, the turbine wake and the hill wake show considerably obvious separations, and the wind deficit follows the streamline starting from the rotor center obtained in the absence of the wind turbine.
2. As the distance from the wind turbine to the hill is reduced, the interactions become stronger, and the recovery of the wind deficit is quicker. For the turbine with $h/H - 1$ mounted at the hilltop, the turbine wake and the hill wake show almost a full mixture; a large-scale wavy structure appears downstream the wind turbine.
3. The change in the terrain shape from a 3D hill to a 2D hill influences the wind fields downstream the wind turbine and the hill. First, the wind speed-up at the hill summit is enhanced for the 2D hill. Second, the interaction is reduced for the 3D hill.

4. The location of the wake center almost follows the streamline starting from the rotor center when the wind turbine is safely upstream of the hill ($\Delta x > 2.5\ H$). The superposition of the wind deficit needs to be added along the streamline starting from the rotor center obtained in the absence of the wind turbine, instead of from the location with a vertical distance $h$ to the local ground.
5. The difference between the wake center and the streamline starting from the center of the rotor obtained in the absence of the wind turbine increases as $\Delta x$ decreases, as $h/H$ decreases, or when changing the terrain shape from 3D hill to 2D hill. Furthermore, the difference between the mean streamwise velocity obtained using the B-line superposition method and that of the directly modeled flow fields is less than 20% when the wind turbine with $h/H = 2.5$ is mounted 2 $L$ upstream of the hills. At $x = 0$, as the most typical installations, the superposition based on B-line fails, and the errors reaches more than 35%.

Although the present LES evaluates the geometrical parameters in a narrow range, the trends of the key parameters in the flow interactions between the wind turbine and the hill are clear. The stratification condition[61,62] and the hill slope,[63] which play important roles in flow interactions, are not considered in this study and should be examined in the near future. Conditions under which the superposition method can be adopted should be further verified by observation of real wind farms in complex terrain. The extent of the difference when different superposition methods are adopted to optimize the wind turbine locations in complex terrain is another topic that should be investigated further. More importantly, for real topographies, the upstream hills would disturb the flow fields over the downstream hills. Due to the additional turbulence caused by the upstream hills in the real complex topographies, the wake effects from the turbine and the hill will show stronger mixing effects; as a result, the flow behind the turbine will recover the ambient flow quickly, and the accuracy of the superposition method proposed in the present study may decrease. Therefore, the application of the present results should be limited in a narrow range of the real topographies, such as an isolated ridge or an isolated hill.

## ACKNOWLEDGEMENTS

Supports from the National Natural Science Foundations of China (51978307) and the Project of Innovation-driven Plan in Huazhong University of Science and Technology (2017KFYXJJ141) are gratefully acknowledged.

## NOMENCLATURE

| | |
|---|---|
| $a$ | axial induced factor |
| $a'$ | tangential induced factor |
| $B$ | number of blades |
| $c$ | chord length [m] |
| $C_D$ | drag force coefficient |
| $C_L$ | lift force coefficient |
| $d$ | distance to the closest wall [m] |
| $dF_D$ | drag force on the blade element [N] |
| $dF_L$ | lift force on the blade element [N] |
| $f_i$ | source term in N–S equation [N m$^{-3}$] |
| $h$ | hub-height [m] |
| $H$ | height of the hill [m] |
| $I$ | turbulence intensity |
| $I_{G_n}$ | turbulence density at the grid level n |
| $L$ | radius of the hill [m] |
| $L_s$ | SGS mixing length [m] |
| $L_{u,x}$ | integral length scale [m] |
| $\tilde{p}$ | filtered pressure [N m$^{-2}$] |
| $r$ | radial location [m] |
| $\tilde{S}_{ij}$ | rate-of-strain tensor |
| $U$ | time-averaged streamwise velocity [m s$^{-1}$] |
| $U_0$ | incoming wind velocity [m s$^{-1}$] |
| $U_{G_n}$ | mean streamwise velocity at the grid level n [m] |
| $U_n$ | axial velocity at the local blade element [m s$^{-1}$] |
| $U_{ref}$, | reference velocity [m s$^{-1}$] |
| $U_\theta$ | tangential velocity at the local blade element [m s$^{-1}$] |
| $\tilde{u}_i$ | filtered velocities [m s$^{-1}$] |

$u_*$ friction velocity [m $s^{-1}$]
$V$ relative velocity respecting to the blade element [m $s^{-1}$]
$x, y, z$ Cartesian coordinates [m]
$z_0$ surface roughness length [m]
$z_s$ shape of the topographies [m]

## GREEKS

$\alpha$ angle of attack [°]
$\alpha_0$ power-law exponent for the mean streamwise velocity
$\gamma$ local pitch angle [°]
$\delta_{ij}$ Kronecker delta
$\delta_n$ distance between the cell center and the wall [m]
$\Delta t$ time step size [s]
$\Delta t^*$ convective time units
$\Delta x$ distance between the wind turbine and the hill [m]
$\Delta_{\chi i}$ grid size [m]
$\epsilon_I$ relative errors of the mean streamwise velocities
$\epsilon_U$ relative errors of the mean streamwise velocities
$\epsilon_{U_B}$ relative errors of B-line method
$\epsilon_{U_D}$ relative errors of D-line method
$\theta$ tangential direction
$\kappa$ von Kármán constant
$\lambda$ tip speed ratio
$\mu$ air viscosity [Pa·s]
$\mu_t$ SGS turbulent viscosity [Pa·s]
$\rho$ air density [kg $m^{-3}$]
$\tau_{ij}$ SGS stress [N $m^{-2}$]
$\varphi$ angle between the relative velocity and the rotor plane [°]
$\Phi$ azimuthal angle [°]

## ORCID

*Zhenqing Liu* https://orcid.org/0000-0002-3591-334X

## REFERENCES

1. CIConsulting, Investment and forecast report on China wind power equipment industry, 2020–2024, 2020. http://www.ocn.com.cn/reports/1342fenglifadian.shtml
2. National Energy Administration of China, The 13th five-year plan for wind power development, 2016. http://www.nea.gov.cn/2016-11/29/c_135867633.htm
3. Taylor G, Smith D. Wake measurements over complex terrain. In: Quarton DC, Fenton VC, eds. *Proceedings of the 13th British Wind Energy Association (BWEA) Conference*. Swansea, UK: Wind Energy Conversion; 1991:335-342.
4. Englberger A, Dörnbrack A. Wind-turbine wakes responding to stably stratified flow over complex terrain. *J Phys: Conf Series*. 2018;1037:072014. https://doi.org/10.1088/1742-6596/1037/7/072014
5. Hyvärinen A, Segalini A. Effects from complex terrain on wind-turbine performance. *J Energy Resour Technol*. 2017;139(5):051205. https://doi.org/10.1115/1.4036048
6. Astolfi D, Castellani F, Terzi L. A study of wind turbine wakes in complex terrain through RANS simulation and SCADA data. *J sol Energy Eng*. 2018;140(3). https://doi.org/10.1115/1.4039093
7. Castellani F, Astolfi D, Mana M, Piccioni E, Becchetti M, Terzi L. Investigation of terrain and wake effects on the performance of wind farms in complex terrain using numerical and experimental data. *Wind Energy*. 2017;20(7):1277-1289. https://doi.org/10.1002/we.2094
8. Hyvärinen A, Lacagnina G, Segalini A. A wind-tunnel study of the wake development behind wind turbines over sinusoidal hills. *Wind Energy*. 2018;21(8):605-617. https://doi.org/10.1002/we.2181
9. Tian W, Ozbay A, Hu H. An experimental investigation on the aeromechanics and wake interferences of wind turbines sited over complex terrain. *J Wind Eng Ind Aerod*. 2018;172:379-394. https://doi.org/10.1016/j.jweia.2017.11.018
10. Howard K, Chamorro P, Guala M. A comparative analysis on the response of a wind-turbine model to atmospheric and terrain effects. *Bound-Lay Meteorol*. 2016;158(2):229-255. https://doi.org/10.1007/s10546-015-0094-9
11. Kozmar H, Allori D, Bartoli G, Borri C. Complex terrain effects on wake characteristics of a parked wind turbine. *Eng Struct*. 2016;110:363-374. https://doi.org/10.1016/j.engstruct.2015.11.033

12. Kozmar H, Allori D, Bartoli G, Borri C. Wind characteristics in wind farms situated on a hilly terrain. *J Wind Eng Ind Aerod*. 2018;174:404-410. https://doi.org/10.1016/j.jweia.2018.01.008
13. Subramanian B, Chokani N, Abhari R. Aerodynamics of wind turbine wakes in flat and complex terrains. *Renew Energy*. 2016;85:454-463. https://doi.org/10.1016/j.renene.2015.06.060
14. Han X, Liu D, Xu C, Shen W. Atmospheric stability and topography effects on wind turbine performance and wake properties in complex terrain. *Renew Energy*. 2018;126:640-651. https://doi.org/10.1016/j.renene.2018.03.048
15. Gao X, Wang T, Li B, et al. Investigation of wind turbine performance coupling wake and topography effects based on LiDAR measurements and SCADA data. *Appl Energy*. 2019;255:113816. https://doi.org/10.1016/j.apenergy.2019.113816
16. Sun H, Gao X, Yang H. Validations of three-dimensional wake models with the wind field measurements in complex terrain. *Energy*. 2019;189:116213. https://doi.org/10.1016/j.energy.2019.116213
17. Sun H, Yang H. Study on an innovative three-dimensional wind turbine wake model. *Appl Energy*. 2018;226:483-493. https://doi.org/10.1016/j.apenergy.2018.06.027
18. Politis E, Prospathopoulos J, Cabezon D, Hansen K, Chaviaropoulos P, Barthelmie R. Modeling wake effects in large wind farms in complex terrain: the problem, the methods and the issues. *Wind Energy*. 2012;15(1):161-182. https://doi.org/10.1002/we.481
19. Makridis A, Chick J. Validation of a CFD model of wind turbine wakes with terrain effects. *J Wind Eng Ind Aerod*. 2013;123:12-29. https://doi.org/10.1016/j.jweia.2013.08.009
20. Nedjari H, Guerri O, Saighi M. CFD wind turbines wake assessment in complex topography. *Energ Conver Manage*. 2017;138:224-236. https://doi.org/10.1016/j.enconman.2017.01.070
21. Shamsoddin S, Porté-Agel F. Large-eddy simulation of atmospheric boundary-layer flow through a wind farm sited on topography. *Bound-Lay Meteorol*. 2017;163(1):1-17. https://doi.org/10.1007/s10546-016-0216-z
22. Murali A, Rajagopalan R. Numerical simulation of multiple interacting wind turbines on a complex terrain. *J Wind Eng Ind Aerod*. 2017;162:57-72. https://doi.org/10.1016/j.jweia.2017.01.005
23. Yang X, Pakula M, Sotiropoulos F. Large-eddy simulation of a utility-scale wind farm in complex terrain. *Appl Energy*. 2018;229:767-777. https://doi.org/10.1016/j.apenergy.2018.08.049
24. Yan S, Shi S, Chen X, Wang X, Mao L, Liu X. Numerical simulations of flow interactions between steep hill terrain and large scale wind turbine. *Energy*. 2018;151:740-747. https://doi.org/10.1016/j.energy.2017.12.075
25. Qian G, Ishihara T. Numerical study of wind turbine wakes over escarpments by a modified delayed detached eddy simulation. *J Wind Eng Ind Aerod*. 2019;191:41-53. https://doi.org/10.1016/j.jweia.2019.05.004
26. Shamsoddin S, Porte-Agel F. Wind turbine wakes over hills. *J Fluid Mech*. 2018;855:671-702. https://doi.org/10.1017/jfm.2018.653
27. Liu Z, Ishihara T, Tanaka T, He X. LES study of turbulent flow fields over a smooth 3-D hill and a smooth 2-D ridge. *J Wind Eng Ind Aerod*. 2016;153:1-12. https://doi.org/10.1016/j.jweia.2016.03.001
28. Liu Z, Ishihara T, He X, Niu H. LES study on the turbulent flow fields over complex terrain covered by vegetation canopy. *J Wind Eng Ind Aerod*. 2016;155:60-73. https://doi.org/10.1016/j.jweia.2016.05.002
29. Liu Z, Cao S, Liu H, Ishihara T. Large-eddy simulations of the flow over an isolated three-dimensional hill. *Bound-Lay Meteorol*. 2019;170(3):415-441. https://doi.org/10.1007/s10546-018-0410-2
30. Liu Z, Diao Z, Ishiraha T. Study of the flow fields over simplified topographies with different roughness conditions using large eddy simulations. *Renew Energy*. 2019;136:968-992. https://doi.org/10.1016/j.renene.2019.01.032
31. Liu Z, Hu Y, Fan Y, Wang W, Zhou Q. Turbulent flow fields over a 3D hill covered by vegetation canopy through large eddy simulations. *Energies*. 2019;12(19):3624. https://doi.org/10.3390/en12193624
32. Liu Z, Hu Y, Wang W. Large eddy simulations of the flow fields over simplified hills with different roughness conditions, slopes, and hill shapes: a systematical study. *Energies*. 2019;12(18):3413. https://doi.org/10.3390/en12183413
33. Burton T, Sharpe D, Jenkins N, Bossanyi E. *Wind Energy Handbook, Second Ed*. Wiley; 2011.
34. Ishihara T, Qian G. A new Gaussian-based analytical wake model for wind turbines considering ambient turbulence intensities and thrust coefficient effects. *J Wind Eng Ind Aerod*. 2018;177:275-292. https://doi.org/10.1016/j.jweia.2018.04.010
35. Ishihara T, Hibi K, Oikawa S. A wind tunnel study of turbulent flow over a three-dimensional steep hill. *J Wind Eng Ind Aerod*. 1999;83(1-3):95-107. https://doi.org/10.1016/S0167-6105(99)00064-1
36. Ishihara T, Fujino Y, Hibi K. A wind tunnel study of separated flow over a two-dimensional ridge and a circular hill. *J Wind Eng*. 2001;89:573-576.
37. Wu Y, Porté-Agel F. Large-eddy simulation of wind-turbine wakes: evaluation of turbine parametrisations. *Bound-Lay Meteorol*. 2011;138(3):345-366. https://doi.org/10.1007/s10546-010-9569-x
38. Ansys Inc. *ANSYS Fluent Theory Guide*. PA: Canonsburg; 2014.
39. Courant R, Friedrichs K, Lewy H. Über die partiellen differenzengleichungen der mathematischen physik. *Math Annal (in German)*. 1928;100(1):32-74. https://doi.org/10.1007/BF01448839
40. Hunt J, Snyder W. Experiments on stably and neutrally stratified flow over a model three-dimensional hill. *J Fluid Mech*. 1980;96(4):671-704. https://doi.org/10.1017/S0022112080002303
41. Finnigan J, Raupach R, Bradley E, Aldis G. A wind tunnel study of turbulent flow over a two-dimensional ridge. *Boundary-Layer Meteorol*. 1990;50(1-4):277-317. https://doi.org/10.1007/BF00120527
42. Cao S, Tamura T. Experimental study on roughness effects on turbulent boundary layer flow over a two-dimensional steep hill. *J Wind Eng Ind Aerod*. 2006;94(1):1-19. https://doi.org/10.1016/j.jweia.2005.10.001
43. Cao S, Tamura T. Effects of roughness blocks on atmospheric boundary layer flow over a two-dimensional low hill with/without sudden roughness change. *J Wind Eng Ind Aerod*. 2007;95(8):679-695. https://doi.org/10.1016/j.jweia.2007.01.002
44. Gong W, Ibbetson A. A wind tunnel study of turbulent flow over model hills. *Bound-Lay Meteorol*. 1989;49(1-2):113-148. https://doi.org/10.1007/BF00116408
45. Dupont S, Brunet Y. Edge flow and canopy structure: a large-eddy simulation study. *Bound-Lay Meteorol*. 2008;126(1):51-71. https://doi.org/10.1007/s10546-007-9216-3

46. Iizuka S, Kondo H. Performance of various sub-grid scale models in large-eddy simulations of turbulent flow over complex terrain. *Atmos Environ*. 2004;38(40):7083-7091. https://doi.org/10.1016/j.atmosenv.2003.12.050
47. Iizuka S, Kondo H. Large-eddy simulations of turbulent flow over complex terrain using modified static eddy viscosity models. *Atmos Environ*. 2006;40(5):925-935. https://doi.org/10.1016/j.atmosenv.2005.10.014
48. Cao S, Wang T, Ge Y, Tamura Y. Numerical study on turbulent boundary layers over two-dimensional hills-effects of surface roughness and slope. *J Wind Eng Ind Aerod*. 2012;104-106:342-349. https://doi.org/10.1016/j.jweia.2012.02.022
49. Kobayashi H, Pereira F, Siqueira M. Numerical study of the turbulent flow over and in a model forest on a 2D hill. *J Wind Eng Ind Aerod*. 1994;53(3):357-374. https://doi.org/10.1016/0167-6105(94)90091-4
50. Griffiths D, Middleton H. Simulations of separated flow over two-dimensional hills. *J Wind Eng Ind Aerod*. 2010;98(3):155-160. https://doi.org/10.1016/j.jweia.2009.10.011
51. Sajjadi S, Craft T, Feng Y. A numerical study of turbulent flow over a two-dimensional hill. *Int J Num Methods Fluids*. 2015;35(1):1-23.
52. Li D, Street R. Numerical study of the wake structure behind a three-dimensional hill. *J Atmos Sci*. 2003;60:1678-1690. https://doi.org/10.1175/1520-0469(2003)0602.0.CO;2
53. Cook N. Determination of the model scale factor in wind-tunnel simulations of the adiabatic atmospheric boundary layer. *J Wind Eng Ind Aerod*. 1978;2(4):311-321. https://doi.org/10.1016/0167-6105(78)90016-8
54. Tamura T, Okuno A, Sugio Y. LES analysis of turbulent boundary layer over 3D steep hill covered with vegetation. *J Wind Eng Ind Aerod*. 2007;95(9–11):1463-1475. https://doi.org/10.1016/j.jweia.2007.02.014
55. Kim S, Shin H, Joo Y, Kim K. A study of the wake effects on the wind characteristics and fatigue loads for the turbines in a wind farm. *Renew Energy*. 2015;74:536-543. https://doi.org/10.1016/j.renene.2014.08.054
56. Thomsen K, Soerensen P. Fatigue loads for wind turbines operating in wakes. *J Wind Eng Ind Aerod*. 1999;80(1):121-136. https://doi.org/10.1016/S0167-6105(98)00194-9
57. Meng H, Lien F, Li L. Elastic actuator line modelling for wake-induced fatigue analysis of horizontal axis wind turbine blade. *Renew Energy*. 2018;116:423-437. https://doi.org/10.1016/j.renene.2017.08.074
58. Dou B, Guala M, Lei L, Zeng P. Wake model for horizontal-axis wind and hydrokinetic turbines in yawed conditions. *Appl Energy*. 2019;242:1383-1395. https://doi.org/10.1016/j.apenergy.2019.03.164
59. Lopez D, Kuo J, Li N. A novel wake model for yawed wind turbines. *Energy*. 2019;178:158-167. https://doi.org/10.1016/j.energy.2019.04.120
60. eim F, Gravdahl A, Adaramola M. Validation of kinematic wind turbine wake models in complex terrain using actual windfarm production data. *Energy*. 2017;123:742-753. https://doi.org/10.1016/j.energy.2017.01.140
61. El-Askary A, Sakr M, Abdelsalam M, Abuhegazy R. Modeling of wind turbine wakes under thermally-stratified atmospheric boundary layer. *J Wind Eng Ind Aerod*. 2017;160:1-15. https://doi.org/10.1016/j.jweia.2016.11.001
62. Subramanian B, Chokani N, Abhari S. Impact of atmospheric stability on wind turbine wake evolution. *J Wind Eng Ind Aerod*. 2018;176:174-182. https://doi.org/10.1016/j.jweia.2018.03.014
63. Liu Z, Wang W, Wang Y, Ishihara T. Large eddy simulations of slope effects on flow fields over isolated hills and ridges. *J Wind Eng Ind Aerod*. 2020;201:104178. https://doi.org/10.1016/j.jweia.2020.104178


**How to cite this article:** Liu Z, Lu S, Ishihara T. Large eddy simulations of wind turbine wakes in typical complex topographies. *Wind Energy*. 2020;1–30. https://doi.org/10.1002/we.2606